

# A new method for estimating suspended sediment concentrations and deposition rates from satellite imagery based on the physics of plumes<sup>☆</sup>

S.D. Peckham

*INSTAAR, University of Colorado, Boulder 80309-0450, USA*

Received 11 September 2007

---

## Abstract

Sediment plumes are typically easy to identify in satellite imagery and there is a great interest in being able to measure suspended sediment concentrations (SSC) from space or airborne instruments. The standard approach to this problem to date has been to try to determine the spectral signatures of different suspended particle mixtures, either empirically or theoretically, and to thereby develop transfer functions that convert multi-band reflectances to SSC. Although this approach has met with some success, there is not yet a robust and accurate algorithm to quantify SSC in plumes in the nearshore environment under varying conditions. This paper describes a completely different and therefore complementary approach to this problem that is based in the hydrodynamics of turbulent 2D jets and the manner in which sediment concentration must decrease along the centerline of a plume. The only data requirement is a measurement or estimate of initial sediment concentrations by grain size at the river mouth. The end result is a transfer function derived from the physics of plumes that allows pixels in remotely sensed images of plumes to be assigned absolute SSC values by particle size in units of  $\text{kg}/\text{m}^3$ . This paper therefore has the following key goals: (1) to review and extend known results for 2D turbulent jets and sediment plumes, (2) to derive bounds for how SSC must decrease along the centerline of a plume and (3) to show how these results can be used to assign SSC values in sediment plume images. Applications and efforts to validate this approach will be presented in a companion paper.

© 2008 Elsevier Ltd. All rights reserved.

*Keywords:* Turbulent jet; Sediment plume; Analytic solutions; Eddy viscosity; Coriolis effect; Satellite image

---

## 1. Introduction

Plumes of suspended particulates (sediment and biological) are readily visible in spectral imagery of the oceans and coastal zones. To even the casual observer they result from river sediment discharges,

wave and tidal erosion of the seabed or shorelines, pelagic “blooms” and spawnings, aeolian dust clouds and human activities. Because they are so obvious, much effort has been put into obtaining the particulate loads (concentrations) in absolute terms such as  $\text{kg}/\text{m}^3$ . For the most part these efforts have employed the deterministic and statistical tools of spectral analysis, which rests on the assumption that different components will have an identifiable spectral signature in reflectance. The premise of

---

<sup>☆</sup> Code available from server at <http://www.iamg.org/CGEditor/index.htm>

E-mail address: [Scott.Peckham@colorado.edu](mailto:Scott.Peckham@colorado.edu)

Nomenclature			
$a$	local constant, as needed	$u$	$x$ -component of velocity field
$A$	an unknown function, as needed	$u_0$	$u$ at river mouth center
$b$	local constant, as needed	$u_1$	cross-flow velocity, Appendix B
$B$	an unknown function, as needed	$u_c$	$u$ on jet centerline, see Section 3.3
$b_0$	river mouth width	$u_i$	$u$ in the inner zone
$c$	local constant, as needed	$t$	time
$c_k$	local constant, as needed (integer $k$ )	$T$	period, inertial circle motion
$C$	depth-averaged suspended sediment concentration	$U$	characteristic velocity
$C_0$	$C$ at river mouth center	$v$	$y$ -component of velocity field
$C_1$	Albertson experimental constant (not a concentration)	$v_0$	an initial value of $v$
$C_d$	drag coefficient, see Appendix B	$v_i$	$v$ in the inner zone
$C_k$	$C$ for the $k$ th grainsize class	$w$	see Eq. (3.23)
$d$	depth, for buoyant plume or river mouth	$x$	offshore distance, Cartesian coordinate
$D$	suspended sediment grainsize, $\mu\text{m}$	$x_0$	$x$ at the river mouth center
$f$	density function or the Coriolis parameter, $2\Omega \sin(\phi)$ , $\text{s}^{-1}$	$x_1$	$x$ at center of inertial circle
$F$	function in similarity solution, see Section 3.6	$x_a$	dimensionless length of inner zone, a multiple of $b_0$
$G$	an unknown function, as needed	$x_m$	$x$ at center of Coriolis spiral
$i, j, k$	integer indices, as needed	$y$	longshore distance, Cartesian coordinate
$I$	inventory of suspended sediment	$y_0$	$y$ at the river mouth center
$I_0$	$I$ at river mouth center	$y_1$	$y$ at center of inertial circle
$I_k$	$I$ for the $k$ th grainsize class	$y_e$	$y$ at edge of potential core
$J$	an unknown function, as needed	$y_m$	$y$ at center of Coriolis spiral
$K$	turbulent eddy viscosity, a scalar field	$\alpha$	the ratio $u_0/u_1$
$K_i$	$K$ in the inner zone	$\beta$	integral of $[F'(s)]^2$ over all $s$
$\ell$	Prandtl's mixing length	$\eta$	see Section 4.2
$L$	characteristic length scale	$\lambda$	sediment removal rate constant
$M$	total flux of $x$ -momentum	$\lambda_a$	shorthand for $\lambda/\sqrt{x_a}$
$p$	an exponent, see Eq. (4.37)	$\mu$	molecular viscosity
$P$	mean pressure, a scalar field	$\phi$	latitude or parametric curve angle in Section 3.7
$r$	radius or radius of curvature	$\rho$	density of water or sea water
$R$	reflectance, see Eq. (2.1)	$\sigma$	plume spreading constant, such that $s = \sigma y/x$
$s$	similarity variable, $\sigma y/x$	$\tau$	Reynolds-averaged shear stress, $\tau(x, y) = \rho \overline{u'v'}$ ,
$s_0$	nonzero $s$ -value such that $v(x, s_0) = 0$	$\zeta$	distance along centerline of a deflected jet
		$\Omega$	angular velocity of earth, $\text{s}^{-1}$
		$\zeta$	vorticity, $v_x - u_y$ , a scalar field

these methods—that distinct mixtures have distinct spectral signatures—implies that they are sensitive to the details of the mixture. Unfortunately, this sensitivity also implies that results for one setting are typically not very portable to other settings, so extensive field calibrations are required for each application. The method to be described in this paper is much less dependent on the composition of the particles in suspension; it instead depends on the actual (not Stokes) settling velocity of particles and

therefore depends mainly on particle size and the tendency to flocculate. It may therefore be more suitable for applications such as the world-wide monitoring of sediment plumes and computing the global flux of sediment from the land to the ocean.

Remotely sensed images show a snapshot of Nature's solution to the fluid dynamical problem of suspended sediment with a proper integration of all the relevant physics, driving forces and boundary conditions. The primary limitations to using satellite

imagery for suspended sediment concentration (SSC) studies are that: (1) they do not show the full 3D solution but just the upper surface, (2) the full time evolution is not available, just snapshots separated in time and (3) the images show relative SSC values (low vs. high) rather than absolute SSC values in  $\text{kg}/\text{m}^3$ . However, flow patterns over a large nearshore region are primarily 2D as long as the water depth is much less than the size of the region. Because of this, a 2D image of conditions at the ocean surface provides most of the flow geometry of the problem. While numerical simulations can, in principle, also provide the flow geometry, there is a greater degree of uncertainty that (1) all of the relevant processes (e.g. frictional losses) have been well modeled, (2) the boundary and initial conditions used to drive the model are correct and (3) nothing important has been left out. In many cases, the data required to set the boundary and initial conditions for the model may simply be unavailable. Another issue with numerical models is that the time required to model the flow in a region at the same spatial resolution and grid size as a satellite image may be prohibitive.

The main idea of this paper is to couple knowledge of the flow geometry provided by a satellite image with the best-available knowledge regarding the hydrodynamics of turbulent jets and sediment plumes as a means of converting satellite images

into maps of SSC. While instantaneous views of turbulent jets and plumes often appear to be somewhat chaotic, with filamentary structures and vortices that appear and disappear over short timescales, time-averaging (over minutes, hours or even days for large plumes) produces images with a much simpler structure. This kind of time averaging can be applied to satellite images, but is also the key idea behind the Reynolds averaging approach that is widely used to model turbulent flows. Fig. 1 (Walker et al., 2005) shows an image created as the average of several AVHRR images of the large sediment plume in the vicinity of the Mississippi River delta during a high-discharge event in May 1993. Despite the complexities introduced by multiple distributaries and an irregular coastline, this image bears a strong resemblance to known similarity solutions for 2D turbulent jets, as will be seen in later sections.

This paper introduces a novel technique for deriving SSC from satellite images that employs known and empirically verified solutions to the Reynolds-averaged equations that govern turbulent jets and plumes. The only information required to apply this technique are (1) an image of relative SSC values derived from remotely sensed reflectance data and (2) measurements at a river mouth in the image, including width, depth, velocity and initial concentrations as a function of particle size.

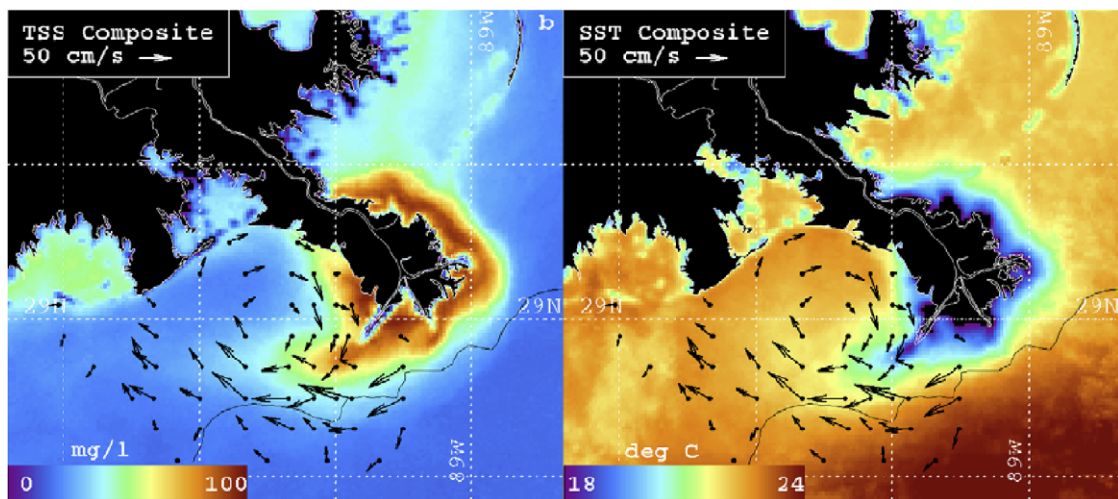


Fig. 1. NOAA AVHRR satellite images of (a) TSS and (b) SST, overlain with ADCP surface current vectors, for a Phase II northeast wind period in April 1994. Velocity scale is standardized and is shown in top left corner of each image. Total suspended solid (TSS) concentrations range from  $0 \text{ mg L}^{-1}$  (blue) to  $100 \text{ mg L}^{-1}$  (orange; see color wedges on imagery). Sea surface temperatures (SST) range from 18 to  $24^\circ\text{C}$ . A one-half degree latitude/longitude grid and a 100-m-depth contour are shown. (Copyright ©2005 Coastal Education and Research Foundation. From Journal of Coastal Research, by Walker et al., 2005. Reprinted by permission of Alliance Communications Group, a division of Allen Press, Inc.)

The method also requires a knowledge of the *removal rate constant* for each type of suspended particle (related to the settling velocity), which in the case of sediment particles are believed to be relatively well constrained by measurements and portable between settings. It will be seen that because the particles are not passive scalars (like salinity), the rate at which they are deposited and therefore removed from the water column plays a key role in the prediction of SSC. Note that calibration and information regarding the satellite sensor are not required.

This paper is organized as follows. Section 2 reviews some existing methods for deriving SSC from reflectance data. Section 3 provides a fairly detailed review of existing mathematical models for 2D turbulent jets and introduces some new results that place existing solutions in the context of a more general framework. Section 4 reviews a sediment plume model that is based on 2D turbulent jet models. A simplified and general form of the model is presented as a parabolic partial differential equation (PDE) with nonconstant coefficients, and several special case solutions are discussed. Methods for obtaining bounds and a closed-form approximation to the *centerline inventory* (the vertically integrated concentration) are then given, with additional results given in Appendix A. A numerical approach to solving the 2D plume equation is also reviewed. In Section 5, it is shown how knowledge of the centerline inventory can be used to assign SSC values for every pixel in a satellite image. Applications and validation of the method will be presented in a companion paper. The key goal of the current paper is to lay the mathematical groundwork for the method. The focus here is on analytic, closed-form solutions to the equations that govern turbulent jets and sediment plumes. It will be seen that a study of these solutions provides considerable physical insight into different aspects of the problem, such as the role played by the eddy viscosity, which is used to parameterize the turbulent shear stress.

## 2. Existing methods for deriving SSC from images

### 2.1. SSC from calibration curves

The most common and well-studied approach to the problem of mapping SSC values from remotely sensed imagery is to use field and laboratory data from water–sediment mixtures to establish

empirical relationships between reflectance and SSC. Polynomial and logarithmic fitting functions or “calibration curves” are the most commonly used. The use of individual bands for this purpose is problematic because of atmospheric variability, and so band ratio images were used early on (Amos and Alfoldi, 1979) as relative SSC images since the rationing provides some level of atmospheric correction. Over the years, more sophisticated image-processing techniques have been developed to create the relative SSC images, including principal component and eigenvector analysis (Topliss, 1984; Amos and Topliss, 1985; Topliss et al., 1990). Like principal component analysis, spectral mixture analysis utilizes all of the spectral bands that are available for a given remote-sensing instrument. Mertes et al. (1993) applied a linear spectral mixing analysis to Landsat data using endmembers that were derived from the laboratory data of reflectance from water–sediment mixtures reported by Witte et al. (1981). This technique has been further explored by Mertes et al. (1998). These methods, while powerful, still rely on field and/or laboratory data for water–sediment mixtures that are similar to those in the remotely sensed scene. They are also based on the assumption of linear spectral mixing.

### 2.2. SSC from radiative transfer models

Building on earlier theoretical work on simplified radiative transfer models by Gordon et al. (1975) (which appears to stem from earlier pioneering work by Preisendorfer, 1961), Stumpf (1987); Stumpf and Pennock (1989, 1991) proposed a “general optical equation” to relate reflectance to SSC in turbid waters. This equation has the form

$$R(\lambda) = \frac{0.33a}{b + c/n_s} = \frac{0.33an_s}{bn_s + c} \quad (2.1)$$

where  $R$  is reflectance,  $n_s$  is SSC and  $a$ ,  $b$  and  $c$  are all constants that depend on the optical properties of the mixture and the wavelength,  $\lambda$ . The parameters  $a$ ,  $b$  and  $c$  are generally not known; instead Stumpf (1987) determines them from the best fit of the above form to available AVHRR data. Although good fits can be obtained, operational use of this equation depends on the availability of data for estimating the three unknown parameters for each wavelength and component material of interest. The result is that Eq. (1) provides a theoretically justified alternative fitting function

for creating calibration curves but still suffers from the problem that the type of data required is difficult to obtain and may be unavailable. Consequently, this equation may be more useful if it is combined with additional information from an independent method such as the one described in this paper.

### 2.3. SSC from numerical hydrodynamic models

Another powerful way to model SSC in a coastal zone is to employ models that solve the governing mass and momentum equations numerically. These results can then be compared with satellite images as a means of assigning absolute SSC values in the images. However, while satellite images of suspended sediment show us the actual surface flow patterns with the sediment as a tracer, numerical simulations only show approximate flow patterns and therefore have a higher degree of associated uncertainty. In a numerical model, there is always uncertainty as to whether (1) all of the relevant physical processes (e.g. frictional losses at the bed or due to turbulence) have been well modeled, (2) the boundary and initial conditions used to drive the model are correct (e.g. wind, waves, tides and bathymetry) and (3) nothing important has been left out. In many cases, the data required to set the boundary and initial conditions for the model may be unavailable, of poor quality, available only at points instead of spatially or at a coarse resolution. Another issue with numerical models is that the time required to model the flow in a region at the same spatial resolution and grid size as a satellite image may be prohibitive. The method for deriving SSC presented in this paper has many of the advantages of a hydrodynamic approach but without the need to solve the equations numerically.

## 3. A mathematical model for 2D turbulent jets

### 3.1. Governing equations for 2D turbulent jets

The well-known Navier–Stokes equations model the conservation of ( $x$  and  $y$ ) momentum for viscous fluid flows. As shown by Rajaratnam (1976) and Abramovich (1963, pp. 52–56) a Reynolds stress treatment of the Navier–Stokes equations as applied to the problem of 2D, steady-state turbulent flow results in the following equations of motion:

$$uu_x + vu_y = (\tau_y - P_x)/\rho \quad (3.1)$$

$$u_x + v_y = 0. \quad (3.2)$$

The  $y$ -momentum equation becomes simply  $P_y = 0$ , so  $P = P(x)$ . Here,  $u(x, y)$  and  $v(x, y)$  are the mean (time-averaged)  $x$  and  $y$  components of the 2D velocity field,  $\tau(x, y) = \rho \overline{u'v'}$  is the turbulent (Reynolds) shear stress (assumed much larger than the molecular shear stress),  $P(x, y)$  is the mean pressure field,  $\rho$  is the density of water and the subscripts all represent partial derivatives with respect to  $x$  and  $y$ . This common notation for partial derivatives will be used throughout this paper. The  $x$ -axis is taken along the centerline of the jet and the  $y$ -axis perpendicular to it with the origin at the mouth of the jet (the river mouth in our case). Eq. (3.2) expresses conservation of mass for an incompressible fluid. The terms on the left-hand side of (3.1) are the “inertial” or advection terms and represent the momentum carried by the flow from one region to another. The first term on the right-hand side of (3.1) represents the frictional losses. For a laminar flow problem, the shear stress would be given by Newton’s viscosity relation,  $\tau = \mu u_y$ , where  $\mu$  is the dynamic (molecular) viscosity, and these equations would reduce to Prandtl’s well-known boundary-layer equations (see Batchelor, 1988, pp. 302, 308, 343). For turbulent flow problems, the turbulent (Reynolds-averaged) shear stress is typically parameterized by either Prandtl’s well-known mixing length formulation or his eddy viscosity formulation, namely

$$\tau = \rho(lu_y)^2 \quad (3.3)$$

or

$$\tau = \rho K u_y, \quad (3.4)$$

where  $l$  is the mixing length. Using Eq. (3.3) leads to the Tollmien (1926) solution while Eq. (3.4) leads to the Goertler (1942) solution (see Rajaratnam, 1976, pp. 14–21; Abramovich, 1963, pp. 108–109) and to the Albertson et al. (1950) solution (see Sections 3.4 and 3.5). In both formulations (which assume a certain amount of statistical isotropy in the turbulence), momentum losses are modeled as a “diffusion of momentum” with a length scale that is related to the size of the turbulent eddies rather than the molecular length scale that is used in the case of viscous, laminar flow. The scalar field  $K(x, y)$  is known as the *eddy viscosity* and plays the role of a spatially varying diffusion coefficient in the resulting equations.

Note that the pressure gradient term in (3.1) as well as a term of the form  $(Ku_x)_x$  are known to be negligible for the case of a symmetric jet with a centerline that follows the  $x$ -axis. While river plumes can be modeled as turbulent jets, they are typically deflected by the Coriolis force and may also be affected by wind stresses, currents, Kelvin waves and density effects. In the general case, it would be necessary to retain both the  $x$  and  $y$  momentum equations, with the pressure gradient terms and additional terms for wind stress, etc. As with the atmosphere, however, it seems likely that the ocean will maintain an approximate geostrophic balance, so that the Coriolis force and wind stress are almost entirely balanced by pressure gradients while the inertial terms are balanced mainly by the friction terms. Note also that the Coriolis force is a “fictitious” force that would not be present in an inertial reference frame and always acts at right angles to velocity vectors. These observations will be used in Section 3.7 to estimate how the centerline of a river plume should be deflected by the Coriolis force. Known results for how a jet is deflected by a cross-flow are given in Appendix B.

Inserting (3.4) into Eq. (3.1), and assuming that  $P_x = 0$ , we have

$$uu_x + vu_y = (Ku_y)_y. \quad (3.5)$$

Implicit in this turbulent jet model is the assumption that the jet is 2D (sometimes referred to as a “slot jet”) with a uniform thickness that is set by the depth of water at the mouth of the river. It is assumed that the flow is well mixed over this depth, and that there is very little mixing below this depth because the fresh water from the river is less dense than the salt water of the ocean. This results in a pycnocline that typically persists for a great distance from the river mouth. In cases where the concentration of suspended sediment at the river mouth is large enough to make the density comparable to the density of seawater, the plume will plunge to the seafloor. This second type of plume is called *hyperpycnal* vs. *hypopycnal*.

### 3.2. Nondimensional form of the 2D turbulent jet equations

We will be working with nondimensionalized variables throughout this paper which leads to simpler equations and allows us to solve a large set of dynamically similar problems with a single

solution. Keep in mind, however, that these results need to be “re-dimensionalized” when applied to a particular plume. Variables in Eqs. (3.3)–(3.5) (and most subsequent equations in this paper) have been nondimensionalized as follows:

$$x = x'/b_0, \quad y = y'/b_0, \quad u = u'/u_0, \quad v = v'/u_0, \\ I = I'/I_0, \quad K = K'/(u_0 b_0), \quad \lambda = \lambda' b_0/u_0. \quad (3.6)$$

Here,  $u_0$  is the velocity at the river mouth,  $b_0$  is the river mouth width,  $I_0$  is the sediment inventory at the river mouth,  $\lambda$  is the sediment removal rate constant and primes indicate the *dimensional* variables. Note that  $I_0$  and  $\lambda$  will be discussed in Section 4. As a result of (3.6), the edges of the river mouth are at  $y = \pm 1/2$  and  $u = 1$  at the river mouth. An alternate method to nondimensionalize the equations of motion is given by

$$x = x'(\lambda/u_0), \quad y = y'/b_0, \quad u = u'/u_0, \quad v = v'/(b_0 \lambda), \\ I = I'/I_0, \quad K = K'/(b_0 \lambda^2), \quad \lambda = \lambda' b_0/u_0. \quad (3.7)$$

It will be seen in Section 4 that method (3.6) leads to Eq. (4.2), which can be solved numerically. Even though (4.2) is nondimensional, it must be solved again whenever a new value of  $\lambda$  is encountered. However, if (3.7) is used instead of (3.6), then instead of (4.2) we get the equation obtained from (4.2) by setting  $\lambda = 1$ . This would appear to offer a major advantage since it would only be necessary to solve that PDE once and then rescale the result using the measured values that appear in (3.7) to obtain a solution for any parameter set,  $u_0$ ,  $b_0$ ,  $I_0$  and  $\lambda$ . Unfortunately, the author encountered numerical problems when trying to solve the alternate version of (4.2) that remain unresolved.

### 3.3. Velocity on the centerline

The following well-known line of reasoning can be used to determine how the  $u$ -component of velocity varies along the centerline of a turbulent jet. (By symmetry, the  $v$ -component is simply zero.) By adding the product of  $u$  and the continuity equation (3.2) to the 2D jet momentum equation (3.5), it can alternately be written in *conservative form* as

$$(u^2)_x + (uv)_y = (Ku_y)_y. \quad (3.8)$$

Integrating each term in this equation from  $y = -\infty$  to  $\infty$ , the terms with the  $y$ -derivatives drop out (since  $uv$  and  $Ku_y$  are both zero at the limits of  $y$ )



and we find that

$$\int_{y=-\infty}^{\infty} (u^2)_x dy = \left[ \int_{y=-\infty}^{\infty} u^2 dy \right]_x = 0. \quad (3.9)$$

It follows that

$$\int_{y=-\infty}^{\infty} u^2 dy = M \quad (3.10)$$

where  $M$  is a constant which represents the total flux of momentum across every line of constant  $x$ , which is the total amount that exits the river mouth. In fact, we know that  $M = 1$  since  $u$  and the river width are nondimensional and both are equal to 1 at the river mouth. Now empirical observations have shown that cross-sections of  $u$  perpendicular to the centerline always have a similar shape, such that the  $u$ -component of velocity has the functional form

$$\frac{u(x, y)}{u_c(x)} = G\left(\frac{\sigma y}{x}\right) \quad (3.11)$$

where  $u_c(x)$  is the  $x$ -component of velocity on the centerline and the function  $G$  is approximately Gaussian. Inserting this into the integral and changing the variable of integration from  $y$  to  $s = \sigma y/x$ , we find that

$$\frac{x u_c^2(x)}{\sigma} \int_{s=-\infty}^{\infty} G^2(s) ds = M. \quad (3.12)$$

The *similarity variable*,  $s$ , is dimensionless and is also equal to  $\sigma \tan(\theta)$ , where  $\theta \in (-\pi/2, \pi/2)$  is the angle between the  $x$ -axis and the ray that points from the origin to the point  $(x, y)$ . The integral here evaluates to a constant,  $\beta$ , and  $M = 1$ , so solving for  $u_c(x)$  we find that

$$u_c(x) = \sqrt{\frac{\sigma}{\beta x}} = \sqrt{\frac{x_a}{x}}. \quad (3.13)$$

This expression agrees well with experimental data and can also be derived from dimensional analysis by recognizing that  $u$  must be a function of  $M$  and  $x$ . It can be seen that  $u_c(x)$  diverges at the origin ( $x = 0$ ), which is known as the *pole* of the turbulent jet. However, the experimental work of Albertson et al. (1950) shows that the similarity of  $u$  profiles does not hold until a distance of more than five river mouth widths ( $x_a \approx 5.2$ ) from the river mouth, and that the centerline velocity is constant up to this point. Note that the dimensional version of (3.13) is  $u'(x') = u_0 \sqrt{x_a b_0/x'}$ . The Albertson solution in Section 3.5 provides an approximate solution in the transitional inner zone.

### 3.4. Goertler's solution for the 2D turbulent jet model

As mentioned previously, Tollmien (1926) determined a solution to the 2D turbulent jet model for the case where Prandtl's "old" mixing-length method is used to parameterize the turbulence, while Goertler (1942) found a solution for the case where the "new" eddy viscosity method is used. These two solutions are similar, however, in that Tollmien assumed that the mixing length,  $l$ , was a function only of  $x$  and Goertler made the same assumption for the eddy viscosity,  $K$ . For more details on Tollmien's solution, which is given in implicit form, see Rajaratnam (1976, pp. 14–21) or Abramovich (1963, pp. 68–76). In this paper we will restrict attention to the now widely used eddy viscosity formulation. Goertler's (dimensional) solution for  $u$ ,  $v$  and  $K$  is

$$u_c = u_0 c \sqrt{\frac{b_0}{x}} \quad (3.14)$$

$$s = \frac{\sigma y}{x} \quad (3.15)$$

$$u = u_c \operatorname{sech}^2(s) \quad (3.16)$$

$$v = \frac{u_c}{\sigma} [s \operatorname{sech}^2(s) - \tanh(s)/2] \quad (3.17)$$

$$K = \frac{u_c x}{4\sigma^2} \quad (3.18)$$

where  $u_c$  is the centerline (and max) velocity as a function of  $x$ ,  $s$  is a generalized coordinate that is constant along lines through the origin,  $c \approx 3.50$  and  $\sigma \approx 7.67$ . (The constants  $c$  and  $\sigma$  were determined from best fits to the experimental data of Reichardt, 1951.) Note that  $K = K(x)$  was assumed. Figs. 2a–d show  $u$ ,  $v$ ,  $K$  and  $\tau$  for this solution.

### 3.5. Albertson's solution for the 2D turbulent jet model

Albertson et al. (1950) took a somewhat different approach which starts with the empirical observation that cross-sections of  $u(x, y)$  perpendicular to the jet centerline are similar to one another and are well fitted by a Gaussian curve. (Goertler's solution is not mentioned by Albertson et al., but is mentioned in comments by reviewers at the end of their paper.) A key aspect of their work was a carefully designed experimental setup that allowed

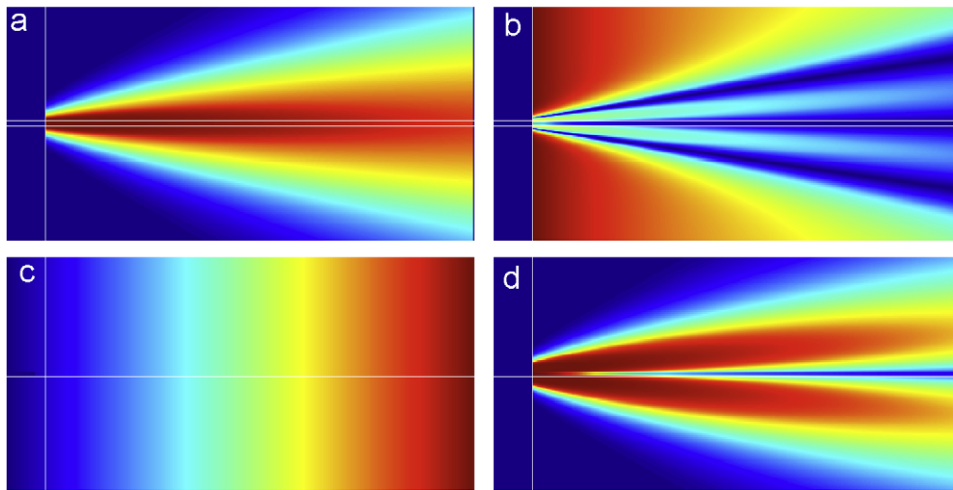


Fig. 2. Goertler's 2D jet solution as images: (a)  $x$ -velocity,  $u$ , (b) absolute value of  $y$ -velocity,  $|v|$ , (c) eddy viscosity,  $K$  and (d) absolute value of Reynolds shear stress,  $|\tau|$ . Note that  $K = K(x)$  in Goertler's jet solution. A white vertical line shows boundary between inner and outer zones and white horizontal lines extend from the edges of river mouth. Here  $x_a = 5.75$ ,  $\sigma = 7.67$  and each image spans 70 river widths. (See Fig. 4.)

them to produce turbulent jets in air (both 2D and 3D) and measure velocities at significant distances (nondimensional  $x$  up to 2000) from the mouth of the jet. Their approach also attempted to address the transitional region in the immediate vicinity of the jet mouth by dividing the flow field into two zones. With  $x$  and  $y$  nondimensionalized by the mouth width, they found that the boundary between the inner and outer zones occurred at  $x = x_a$ , where

$$x_a = \frac{1}{\sqrt{\pi}C_1} \approx 5.176 \quad (3.19)$$

(mouth widths) and  $C_1 \approx 0.109$  is a constant that they determined from their experimental results. The transitional inner zone is called the “zone of flow establishment”, while the outer zone is called the “zone of established flow”. Results for each of these zones are listed in the next two subsections. For flow in fjords, Syvitski et al. (1998) identified a third zone called the “zone of flow confinement” since the plume cannot spread beyond the width of the fjord.

### 3.5.1. The zone of flow establishment

This inner zone ( $x < x_a$ ) is further subdivided into two regions, a wedge-shaped “potential core” region where  $|y| < y_e(x)$  and

$$y_e(x) = [1 - (x/x_a)]/2 \quad (3.20)$$

and the region where  $y > y_e(x)$ . Note that  $y_e(0) = \frac{1}{2}$  and  $y_e(x_a) = 0$ . Within the potential core, we have

$u = 1$ ,  $v = 0$  and  $K = 0$ . Outside of the potential core where  $y > y_e(x)$ , the following expressions provide an approximate solution for the velocity components:

$$u_i(x, y) = \exp(-w^2) \quad (3.21)$$

$$v_i(x, y) = \frac{\text{sgn}(y)}{\sigma} \left[ w e^{-w^2} - \frac{\sqrt{\pi}}{2} \text{erf}(w) + \sqrt{\frac{\pi}{8}} (1 - e^{-w^2}) \right] \quad (3.22)$$

where

$$w(x, y) = \left(\frac{\sigma}{x}\right)[|y| - y_e(x)] \quad (3.23)$$

$$\sigma = \frac{1}{\sqrt{2}C_1} = x_a \sqrt{\frac{\pi}{2}} \quad (3.24)$$

and

$$\text{erf}(x) = \frac{2}{\sqrt{\pi}} \int_{t=-\infty}^x \exp(-t^2) dt. \quad (3.25)$$

The function  $\text{erf}(x)$  is the well-known *error function*. Equivalent expressions are given by Syvitski et al. (1998). Note that cross-sections of  $u$  in the inner zone are equal to 1 for  $y \leq y_e(x)$  and have a Gaussian shape for  $y > y_e(x)$ . However, since  $w(x, y)$  has  $x$  in the denominator it plays a role similar to the standard deviation of the Gaussian curve, and as  $x$  goes to zero,  $u_i(x, y)$  tends towards a square pulse of unit width (see Fig. 3). A solution for the outer zone where  $x > x_a$  will be given in the next section and we will find that the  $u$  expressions



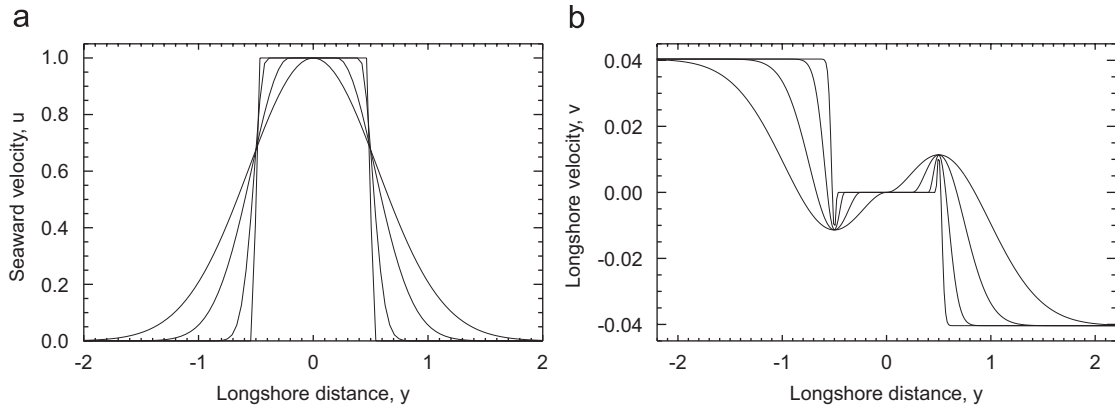


Fig. 3. Cross-sections through inner zone of Albertson's 2D jet model. (a)  $x$ -velocity,  $u$  and (b)  $y$ -velocity,  $v$ .

for the inner and outer zones match at the boundary, so that  $u_i(x_a, y) = u(x_a, y)$  and has the shape of a simple Gaussian curve. It is easily verified that

$$\int_{y=-\infty}^{\infty} u_i^2(x, y) dy = 1 \tag{3.26}$$

for all  $x \leq x_a$  (using the fact that  $\sigma/x_a = \sqrt{\pi/2}$ ) so that  $u_i(x, y)$  satisfies the integral version of momentum conservation discussed in Section 3.3. Moreover,  $u_i(x, y)$  and  $v_i(x, y)$  satisfy the continuity equation. We also have  $v_i(x, y_e(x)) = 0$  so  $v_i$  is continuous across the boundary between the potential core and the rest of the inner zone. However, this approximate solution does not obey  $v_i(x_a, y) = v(x_a, y)$ , so that  $v$  is not continuous across the boundary in this two-zone model. The discontinuity is not severe, though, so that numerical results for  $I(x, y)$  are still smooth across the boundary (see Section 4.4). Although not given in the cited references, it is also possible to integrate the momentum equation with  $u_i$  and  $v_i$  as given above to find an expression for  $K_i$  for use in the inner zone outside of the potential core. The result is

$$K_i(x, y) = \left(\frac{1}{4x_a}\right) \left(\frac{|y| - y_e(x)}{w^2}\right) \{[\sqrt{2} \operatorname{erf}(w) - 1] - e^{w^2} [\operatorname{erf}(\sqrt{2} w) - g(x)]\}. \tag{3.27}$$

Note that if we take  $g(x) = 1$ , then  $K_i(x, y_e(x)) = 0$ , so that if we have  $K = 0$  in the potential core (as commonly assumed), then  $K_i$  is continuous across the boundary between the core and the rest of the inner zone. However, we then find that  $K_i < 0$  for some values of  $x$ ,  $K_i(x_a, y) \neq K(x_a, y)$ , and the shape of the curve in the inner zone does not have the smooth shape of the curve in the outer zone.

The basic reason for discontinuities between inner and outer zones at  $x = x_a$  is that the solution in the outer zone represents a *similarity solution* toward which the solution evolves as  $x$  increases seaward. However, the rate at which the similarity solution is approached must depend on the initial shape of  $u$  at  $x = 0$ , which the Albertson solution takes to be a square pulse of unit height. The extent to which the solutions in the inner and outer zones match is also partly determined by the chosen value of  $x_a$ , which is close to 5.2. The parameter  $\sigma$  determines the spreading angle of the plume in both the inner and outer zones and is proportional to  $x_a$  (see Eq. (3.13)).

3.5.2. The zone of established flow

In the outer zone ( $x > x_a$ ) of a symmetric, turbulent jet, empirical (nondimensionalized) measurements of  $u(x, y)$  can be fit very well by a Gaussian profile (Albertson et al., 1950). As pointed out by Reichardt (1951), a Gaussian profile is to be expected if we view the lateral spread of  $x$ -momentum as a diffusive process. Assuming a profile of this form, and using our previous result for  $u_c(x)$ ,  $u(x, y)$  can be expressed as

$$u_c = \sqrt{\frac{x_a}{x}} \tag{3.28}$$

$$s = \frac{\sigma y}{x} \tag{3.29}$$

$$\sigma = \frac{1}{\sqrt{2} C_1} \tag{3.30}$$

$$u(x, y) = u_c \exp(-s^2). \tag{3.31}$$

A straightforward integration of the equation for mass conservation for this choice of  $u(x, y)$  leads to

an expression for the  $y$ -component of velocity (Syvitski et al., 1998)

$$v(x, y) = \frac{u_c}{\sigma} \left[ s \exp(-s^2) - \frac{\sqrt{\pi}}{4} \operatorname{erf}(s) \right]. \quad (3.32)$$

The velocity field defined by this  $u(x, y)$  and  $v(x, y)$  was used by both Albertson et al. (1950) and Syvitski et al. (1998) as a mathematical model for flow in the zone of established flow. The eddy viscosity,  $K(x, y)$ , that solves the momentum equation with this choice of  $u$  and  $v$  was given graphically by Albertson et al. (1950) and a fit to Albertson’s curve was given by Syvitski et al. (1998). It can be shown, however, that the left-hand side of the momentum equation (for this  $u$  and  $v$ ) can be written as

$$uu_x + v u_y = - \left( \frac{1}{8x_a} \right) [\operatorname{erf}^2(s)]_{yy}. \quad (3.33)$$

Given this fact, the momentum equation becomes easy to integrate and yields the following closed-form expression for the (nondimensional) eddy viscosity

$$K(x, y) = \frac{\sqrt{2}}{8\sigma} \sqrt{\frac{x}{x_a}} \left[ \frac{\operatorname{erf}(s)}{s} \right]. \quad (3.34)$$

On the centerline ( $y = 0$  or  $s = 0$ ) L’Hôpital’s rule can be used to show that

$$K(x, 0) = \frac{1}{4\sigma} \sqrt{\frac{2x}{\pi x_a}}. \quad (3.35)$$

Since  $\sigma \approx 6.5$ , we find that  $K(x_a, 0) \approx 0.03$ . Since  $K_i(x_a, 0) = 0$ , this implies that there is a discontinuity in  $K$  on the centerline at  $x = x_a$ . Plots of  $u$ ,  $v$ ,  $K$  and  $\tau$  for this symmetric jet model are shown in Figs. 4a–d. Cross-sections for  $v$  and  $K$  for different values of  $x$  are shown in Fig. 5.

### 3.6. A more general 2D turbulent jet solution

Comparing the expressions for  $u$  and  $v$  in the Goertler and Albertson (outer zone) solutions, we see that they can both be written in the form

$$u(x, y) = u_c(x) F'(s) \quad (3.36)$$

$$v(x, y) = \frac{u_c(x)}{\sigma} \left[ s F'(s) - \frac{F(s)}{2} \right] \quad (3.37)$$

where  $s(x, y) = \sigma y/x$  and  $\sigma$  is a constant. Requiring  $u_c(x_a) = 1$  in Eq. (3.13) implies that  $\sigma = \beta x_a$ , where  $\beta = \int_{-\infty}^{\infty} [F'(s)]^2 ds$ . For the Goertler solution we have  $F'(s) = \operatorname{sech}^2(s)$ ,  $\beta = 4/3$  and for the Albertson solution we have  $F'(s) = \exp(-s^2)$ ,  $\beta = \sqrt{\pi/2}$ . It turns out that  $u_x + v_y = 0$  for any choice of the function  $F(s)$ . (But we require  $F'(0) = 1$  since  $u$  has been nondimensionalized.) It can also be verified that

$$uu_x + vu_y = \left( \frac{-x_a}{4\sigma^2} \right) [F^2(s)]_{yy}. \quad (3.38)$$

The fact that  $F(s)$  is not uniquely determined by the boundary conditions is a result of introducing the eddy viscosity,  $K$ , to parameterize the Reynolds

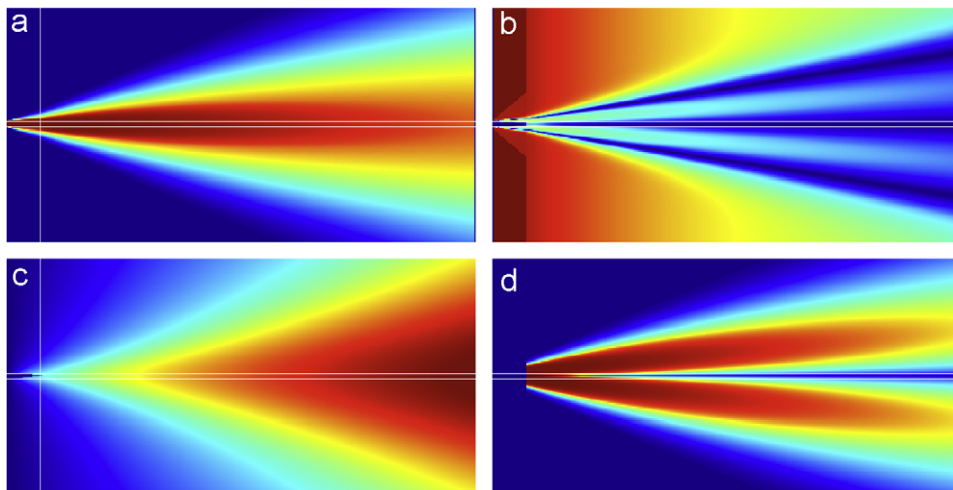


Fig. 4. Albertson’s 2D jet solution as images: (a)  $x$ -velocity,  $u$ , (b) absolute value of  $y$ -velocity,  $|v|$ , (c) eddy viscosity,  $K$  and (d) absolute value of Reynolds shear stress,  $|\tau|$ . A white vertical line shows boundary between inner and outer zones and white horizontal lines extend from edges of river mouth. Here  $x_a = 5.13$ ,  $\sigma = 6.43$  and each image spans 70 river widths.

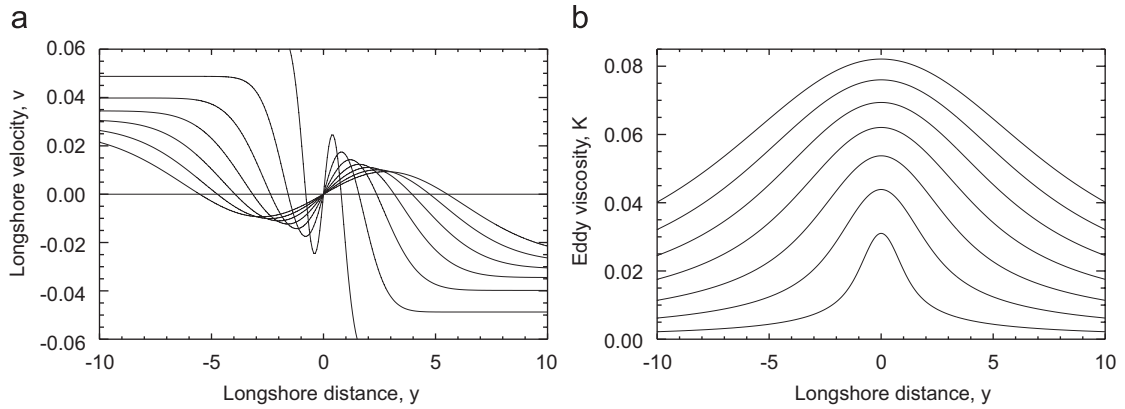


Fig. 5. Cross-sections through outer zone of Albertson's 2D jet model. (a)  $y$ -velocity,  $v$  and (b) eddy viscosity,  $K$ .

shear stress in the turbulent flow field. In the absence of turbulence,  $K$  would be replaced by a material constant, namely the dynamic (molecular) viscosity,  $\mu$ . The number of equations would then equal the number of unknowns and we would not have the freedom to specify  $u(x, y)$ . However, with  $u$  and  $v$  expressed in terms of an arbitrary function,  $F(s)$ , the momentum equation (3.5) can be integrated for  $K$  (via (3.38)) to get

$$K(x, y) = - \left[ \frac{xu_c(x)}{2\sigma^2} \right] \left[ \frac{F(s)F'(s)}{F''(s)} \right] \quad (3.39)$$

$$\tau(x, y) = \rho K u_y = - \left( \frac{\rho}{2\sigma} \right) u_c^2(x) F(s) F'(s). \quad (3.40)$$

Note that if  $F(0) = 0$ , as it does in both the Goertler and Albertson solutions, then the shear stress on the centerline,  $\tau(x, 0)$ , is also equal to zero. The vorticity,  $\zeta = v_x - u_y$ , can also be expressed in terms of  $u_c(x)$  and  $F(s)$  and is given by

$$\zeta(x, y) = \frac{-u_c(x)}{\sigma x} \left[ (\sigma^2 + s^2) F''(s) + s F'(s) - \frac{F(s)}{4} \right]. \quad (3.41)$$

For the plume centerline ( $y = 0$  or  $s = 0$ ), we have  $F'(0) = 1$  (since the equations are nondimensional) and  $F''(0) = 0$  (since the velocity is maximum at  $s = 0$ ), and we can again use L'Hôpital's rule to show that

$$K(x, 0) = - \left[ \frac{xu_c(x)}{2\sigma^2} \right] \left[ \lim_{s \rightarrow 0} \{ F'''(s) \} \right]^{-1}. \quad (3.42)$$

Since  $u_c(x) = \sqrt{x_a/x}$ , we always have  $K(x, 0) = c_k \sqrt{x}$ , where  $c_k$  is a constant that depends on the

choice  $F(s)$ . For the Goertler solution we have

$$F(s) = \tanh(s) \quad (3.43)$$

$$F'(s) = \text{sech}^2(s) \quad (3.44)$$

$$F''(s) = -2 \text{sech}^2(s) \tanh(s) \quad (3.45)$$

$$F'''(s) = 2[\cosh(2s) - 2] \text{sech}^4(s) \quad (3.46)$$

so that the  $F$  term in (3.39) simplifies to  $-\frac{1}{2}$  and we have  $K = K(x)$ . This appears to be the only solution where  $K$  has no  $y$ -dependence. For the Albertson solution we have

$$F(s) = \frac{\sqrt{\pi}}{2} \text{erf}(s) \quad (3.47)$$

$$F'(s) = \exp(-s^2) \quad (3.48)$$

$$F''(s) = -2s \exp(-s^2) \quad (3.49)$$

$$F'''(s) = 2(2s^2 - 1) \exp(-s^2). \quad (3.50)$$

Interestingly, even though  $F(s)$  is an even function (symmetric about the centerline) for the Goertler and Albertson solutions, the mass and momentum equations are satisfied for any  $F(s)$ , even those that are asymmetrical. In every case we will have  $u_c(x) = \sqrt{x_a/x}$ , since this was shown to follow whenever  $u$  takes the form of Eq. (3.11).

### 3.6.1. Oscillations in cross-sections of $v$

It can be seen from Eq. (3.37) that  $v(x, y)$  generally has three roots, one at  $s = 0$  and two more given by  $s = \pm s_0$ , where  $s_0$  is close to 1. It follows that for any fixed value of  $x$ , the sign of  $v$  will change three times over the full range of  $s$ . The sign of  $v$  is positive (and toward the centerline) for  $s < -s_0$ , negative (and away from the centerline) for  $-s_0 < s < 0$ , positive (and away from the centerline) for  $0 < s < s_0$ , and negative (and toward the centerline) for  $s > s_0$ . The basic reason for this behavior is that the plume must diverge from the centerline but also entrains water as it enters the sea in order to satisfy continuity. This behavior is clearly visible in Fig. 4b.

### 3.7. Coriolis deflection of a 2D turbulent jet

The Rossby number measures the relative importance of the Coriolis effect and is given by

$$Ro = \frac{U}{Lf} \quad (3.51)$$

where  $U$  is a characteristic velocity,  $L$  is a characteristic length scale,  $f = 2\Omega \sin(\phi)$  is the Coriolis parameter,  $\Omega$  is the angular velocity of the earth ( $\Omega = 2\pi/86164 \approx 7.292 \times 10^{-5}$  rad/s), and  $\phi$  is the latitude. (Note that the rotational period of the earth is 4 min less than 24 h.) A Rossby number of 1 indicates that the Coriolis and inertial forces are of the same order, and typical values for river plumes (e.g.  $f \approx 10^{-4}$ ,  $U = 1$  m/s,  $L = 10$  km) give Rossby numbers close to 1. However, there is some freedom in the choice of  $L$ , which may be taken to be a measurement from the plume itself or the width of the river mouth.

If we view the plume solutions given previously as those corresponding to an inertial reference frame, then it seems that we should be able to use our knowledge of how the centerline velocity decreases with distance from the mouth to determine how the centerline will be deflected by the Coriolis force. One approach is to try to extend the concept and equations for *inertial circles* which are well known in meteorology. For more information on the Coriolis effect and inertial circles, see Stommel and Moore (1989), Durran (1993), Persson (1998, 2005), Phillips (2000) and McIntyre (2000).

The idea is to assume that  $f$  is constant in the vicinity of the river mouth at  $(x_0, y_0)$  (the well-known  $f$ -plane approximation) and then solve the pair of equations

$$\frac{du}{dt} = fv \quad (3.52)$$

$$\frac{dv}{dt} = -fu \quad (3.53)$$

to get

$$u(t) = u_0 \cos(ft) + v_0 \sin(ft) \quad (3.54)$$

$$v(t) = v_0 \cos(ft) - u_0 \sin(ft) \quad (3.55)$$

$$x(t) = x_0 + (v_0/f)[1 - \cos(ft)] + (u_0/f) \sin(ft) \quad (3.56)$$

$$y(t) = y_0 - (u_0/f)[1 - \cos(ft)] + (v_0/f) \sin(ft). \quad (3.57)$$

Here, the  $x$ -axis points east and the  $y$ -axis points north. The poles and the equator are special and permit other solutions as discussed in the cited references. If we define  $x_1 = x_0 + v_0/f$  and  $y_1 = y_0 - u_0/f$ , it is easily shown that  $(x - x_1)^2 + (y - y_1)^2 = (u_0^2 + v_0^2)/f^2$ , or that the trajectory is that of a circle centered at  $(x_1, y_1)$  with a radius of  $r = \sqrt{u_0^2 + v_0^2}/f$  and a period of  $T = 2\pi/f$ .

At mid-latitudes,  $f \approx 10^{-4}$ , so a fluid parcel with a constant speed of 1 m/s is predicted to travel in a circle of radius of about 10 km with a period of about 0.7 days. This analysis provides a good approximate solution for objects that travel at constant velocity (i.e.  $u^2 + v^2 = u_0^2 + v_0^2$ ) and do not get too far from the origin (since  $f$  varies with latitude,  $\phi$ ). It also properly neglects the centrifugal force, since its horizontal component is balanced by the horizontal component of gravity on an oblate spheroid (like earth) and its vertical component is incorporated into the definition of the gravitational constant (Durran, 1993). It is frequently said in meteorology that the effect of the Coriolis force acting alone is to return a fluid parcel to its starting point. In the case of river plumes, however, once the trajectory has turned to point back toward the shoreline it is constrained to follow the shoreline and the Coriolis force will cause it to stay close, creating a coastal current. As discussed by Fong and Geyer (2002), an unsteady “bulge” is also sometimes formed near the river mouth, although not as pronounced in observations as in numerical simulations.

As shown above, the inertial circle trajectories are for fluid parcels that travel at a constant speed (as measured by an observer on the rotating earth) in the absence of pressure gradients and other forces. From the results of Section 3.3, however, we know that the velocity on the centerline of a plume is not constant, but gradually decreases with distance



from the mouth according to  $u = dx/dt = c/\sqrt{x}$ , where  $c = u_0\sqrt{x_a b_0}$ . Integrating, we find that

$$x(t) = \left(\frac{3ct}{2}\right)^{2/3} \tag{3.58}$$

$$u(t) = c^{2/3} \left(\frac{3t}{2}\right)^{-1/3} \tag{3.59}$$

These two equations give the position and speed of a fluid parcel that starts at  $x = b_0 x_a$  when  $t = t_a$ . Recall that  $x_a \approx 5.2$ . Since the radius of an inertial circle is proportional to the speed (as shown above), we expect that as the parcel slows down the radius of curvature of its trajectory should become smaller.

Fig. 6 from Hitchcock et al. (1997) shows eight drifter trajectories measured at hourly intervals for the peak annual discharge event for the Mississippi River flood of May 1993. This event had a discharge of over  $(30 \times 10^3 \text{ m}^3 \text{ s}^{-1})$  which is more than twice the 63-year mean for the month of May  $(14 \times 10^3 \text{ m}^3 \text{ s}^{-1})$  and about 50% larger than the discharge of the great flood of August 1993  $(20 \times 10^3 \text{ m}^3 \text{ s}^{-1})$ . This image provides a reasonable test case for analyzing the Coriolis effect on river plumes due to (1) the unusually large discharge (about  $30 \times 10^3 \text{ m}^3/\text{s}$ ), (2) the offset of the main

mouth from the shoreline (by about 10 km), (3) the curved shape of the coastline to the west of the main mouth, (4) the light winds from the southeast (as opposed to strong winds from the west during the flood of August 1993) and (5) relatively weak tidal currents (averaging  $15 \text{ cm s}^{-1}$ ) and tidal range (averaging 30 cm; see Murray, 1972). The “main mouth” referred to here is the largest of the three passes in the bird’s foot delta, called Southwest Pass. The latitude and longitude of the delta are about  $29^\circ \text{N}$  and  $89.5^\circ \text{W}$ , respectively. It follows that  $f = 7 \times 10^{-5}$ . Note that  $1^\circ$  of longitude spans a distance of about  $111.1 \cos(\phi) \text{ km}$ , which is about 97.2 km at a latitude of  $29^\circ$ . The initial radius of curvature of the deflected plume can therefore be estimated from Fig. 6 to be about 35 km, while the radius of curvature at a flow distance of 50 km is about 5 km. If we simply assume based on the inertial circle and plume centerline analysis (Section 3.3) that the radius of curvature on the centerline is equal to

$$r(\xi) = \frac{u}{f} = \frac{u_0}{f} \left[ \frac{x_a b_0}{\xi} \right]^{1/2} \tag{3.60}$$

where  $b_0$  is the river mouth width and  $\xi$  is distance along the plume centerline, then these observations allow us to predict that  $u_0 = 2.5 \text{ m/s}$  and  $b_0 = 0.2 \text{ km}$  for the May 1993 event. Note that the Coriolis force cannot change the speed, but only the direction of the velocity vector, so  $\xi$  is simply distance along the plume centerline. The bottom width of Southwest Pass is about 750 ft or 0.14 km (Saucier, 1998). The fact that both of these values are reasonable suggests that (3.60) may provide a fairly good approximation and supports the centerline velocity result from Section 3.3. Recall that the radius of curvature is the inverse of the curvature, or  $r(\xi) = 1/\phi'(\xi)$ , where  $\phi(\xi)$  is the angle that the tangent to a parametric plane curve makes with a fixed  $x$ -axis. Integrating  $\phi'(\xi) = 1/r(\xi)$ , with  $r(\xi)$  given by (3.60) we find that

$$\phi(\xi) = \left(\frac{2}{3c}\right) \xi^{3/2} + \phi_0 \tag{3.61}$$

where  $c = (u_0/f)\sqrt{x_a b_0}$ . The corresponding plane curve can be given parametrically as

$$x(\xi) = x_0 + \int_{t=0}^{\xi} \cos[\phi(t)] dt \tag{3.62}$$

$$y(\xi) = y_0 + \int_{t=0}^{\xi} \sin[\phi(t)] dt. \tag{3.63}$$

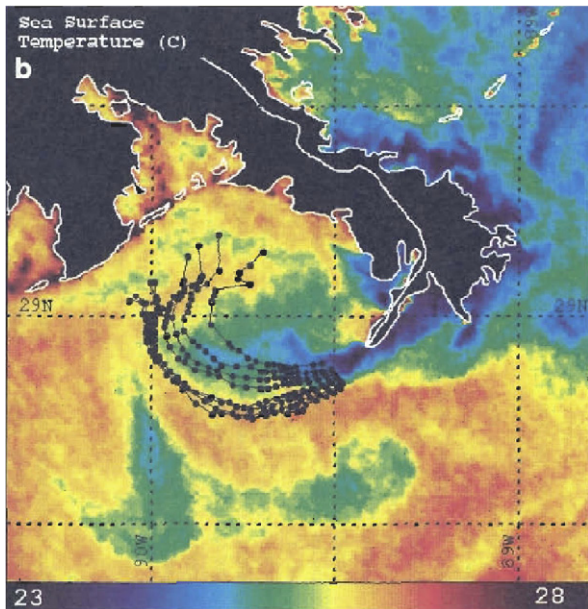


Fig. 6. Eight drifter paths overlain on an image of sea surface temperature for peak annual discharge event of May 1993 for Mississippi River. Note that radius of curvature decreases along a path. (Copyright ©1997 Elsevier. From Hitchcock et al., 1997, used with permission.)



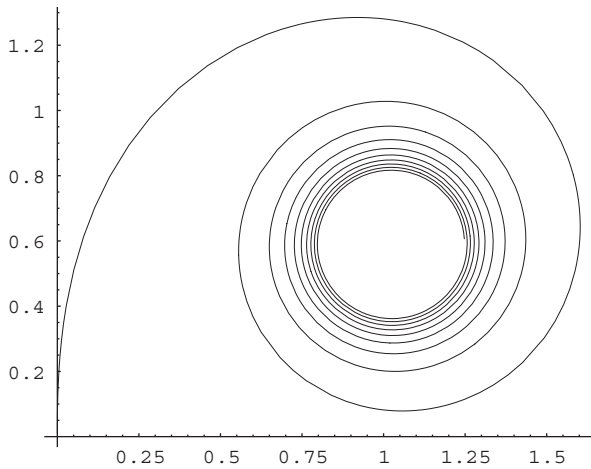


Fig. 7. Spiral curve that is obtained by combining inertial circle concept with centerline velocity result of Section 3.3. Here,  $\phi_0 = \pi/2$ ,  $c = 1$  and  $x$ -axis is shoreline. See Fig. 6.

The integrals can be obtained in terms of the incomplete gamma function using symbolic math software and then plotted. The resulting spiral curve is shown in Fig. 7. The parameter  $\phi_0$  gives the angle that the initial velocity vector makes with the  $x$ -axis. Note that all length scales in this curve are proportional to  $c^{2/3}$ , and that  $c$  depends on  $u_0$ ,  $f$  and  $b_0$ . For example, the center of the spiral occurs at  $x_m = a_1 c^{2/3}$  and  $y_m = a_2 c^{2/3}$ , where  $a_1$  and  $a_2$  are constants that do not depend on  $c$ . With  $\phi_0 = \pi/2$ ,  $y_m$  represents the offshore distance to the center of the “bulge”, which can be compared to the numerical modeling results of Fong and Geyer (2002) and others. The distance along the curve to the point where the angle has turned through  $90^\circ$  ( $\phi(\xi) - \phi_0 = \pi/2$ ) is given by  $\xi_1 = [3\pi c/4]^{2/3}$ . It can also be shown that

$$u(\phi) = f c^{2/3} \left[ \frac{2}{3} (\phi - \phi_0) \right]^{-1/3}. \tag{3.64}$$

This makes it easy to compute how much the speed is reduced for a given change in flow direction. The shape of the curve is very similar to the drifter trajectories shown in Fig. 6. This result should not be over-interpreted, however, since continuity issues arise once the tangent vector becomes perpendicular to the coastline and this may also change the manner in which the speed along the centerline changes with distance. In order to satisfy 2D mass balance it appears necessary for there to be a growing bulge, while 3D mass balance with downwelling may permit a steady solution. For the plume in Fig. 6, most of the suspended sediment is deposited before the flow direction becomes

perpendicular to the shoreline. A more complete analysis will be presented in a subsequent paper.

#### 4. A mathematical model for 2D sediment plumes with deposition

##### 4.1. Governing equation for 2D sediment plumes with deposition

The results of Section 3 are for a 2D turbulent jet model that can be used to model the turbulent flow of water near the mouth of a river. In this section we show how this model can be extended to model the flow of suspended sediment in the water, following Syvitski et al. (1998). It is known that for typical SSCs, the additional mass of the water–sediment mixture is too small to significantly alter the flow of the water. In this case the velocity field for the water–sediment mixture will be the same as for the water alone, and we can also use the same eddy viscosity,  $K$ . The total amount of sediment in a given water column can then be determined by integrating the SSC over the depth of the 2D plume. This depth-integrated mass of sediment per unit area,  $I$ , is called the *inventory* and is related to the plume depth,  $d$ , and *depth-averaged concentration*,  $C$ , by the formula

$$I(x, y) = d(x, y)C(x, y). \tag{4.1}$$

The initial value of the inventory is given by  $I_0 = d C_0$ , where  $I_0 = I(0, 0)$ ,  $C_0 = C(0, 0)$  and  $d$  is the river depth. Here  $I$  and  $C$  may represent values for a given grain size or totals. For sufficiently small concentrations (including typical values of interest), conservation of mass for sediment can be written as

$$uI_x + vI_y + \lambda I = (KI_y)_y. \tag{4.2}$$

Notice that this is an *advection–diffusion equation* with a sink term and is very similar to the equation for the  $x$ -component of momentum in the turbulent jet, except now some of the  $u$ 's have been replaced with  $I$ 's and there is an additional term to model the deposition of sediment on the ocean floor. The constant,  $\lambda$ , has units of inverse time and is called the *removal rate constant*. It is essentially the inverse of the amount of time, on average, that a particle spends within the plume before crossing the lower boundary. It depends on the size, composition, settling velocity and tendency to flocculate of the suspended material. Due to turbulence, however, particle paths are not straight down and it cannot be computed as the quotient of the Stokes settling velocity and plume depth. For a more complete discussion of these issues,

see Syvitski et al. (1985) and Bursik (1995). Eq. (4.2) holds for each component material, so that one could add a subscript  $k$  to both  $I$  and  $\lambda$  in the equation.

A table of empirically determined removal rate constants for different materials and grain sizes was given by Syvitski et al. (1998). These authors also showed the importance of taking flocculation into account. The four pairs of values in their table are: [1.5, 2], [4.8, 2.7], [15.0, 4.7] and [48.0, 12.3], where the first element of each pair is a grainsize in microns, and the second element is the removal rate constant in units of 1/day. Applying a linear regression to these values results in the expression:

$$\lambda(D) = (0.222D) + 1.573 \quad (R^2 = 0.999) \quad (4.3)$$

where  $D$  is grainsize in microns. Based on a physical interpretation of  $\lambda$ , it would seem that  $\lambda$  should also depend on  $d_0$  and  $u_0$ , where  $d_0$  is the river depth at the mouth. If so, then perhaps  $\lambda$  can only be given as a simple function of grainsize if it is first non-dimensionalized as  $\lambda = \lambda' d_0/u_0$ . However, the data collected by Syvitski et al. (1985) suggests that  $\lambda$  values may indeed be universal, or at least weakly dependent on other parameters. This issue merits further investigation in order to ensure that the new method for computing SSC from satellite images proposed in Section 5 is portable between settings.

4.1.1. Sediment inventory in the inner zone

Recall that for the Albertson solution there is a wedge-shaped “potential core” where  $u = u_0$ ,  $v = 0$  and  $K = 0$ . In this region the *nondimensional* 2D plume model simplifies to  $I_x + \lambda I = 0$ , which can be integrated immediately to get

$$I(x, y) = \exp(-\lambda x) \quad (x \leq x_a). \quad (4.4)$$

Notice that the (nondimensional) removal rate constant for the material in question determines the rate of exponential decay. Notice that the free constant from the integration that determines  $I(0, 0)$  has been set to one since this is a solution to the nondimensional equations.

4.1.2. Matching solutions at the zone boundary

The solutions for  $I(x, y)$  in the inner and outer zones must agree at  $x = x_a$ . It follows from the last equation then that  $I(x_a, 0) = \exp(-\lambda x_a)$ . Since the 2D plume model equation is *linear*, we are free to multiply any solution by a constant in order to satisfy this boundary condition. We also know that if  $I_1$  and  $I_2$  are any two solutions then  $I_1 + I_2$  must also be a solution. Any nondimensional outer zone

solution,  $I(x, s) = f(x, s)$ , can be made to match the inner zone solution on the centerline by multiplying by  $c = \exp(-\lambda x_a)/f(x_a, 0)$ .

4.2. Alternate form of the 2D plume model

In Section 3, the Goertler, Albertson and more general turbulent jet solutions were each given in terms of offshore distance,  $x$ , and a *similarity variable*,  $s = \sigma y/x$ . The variable  $y$  did not appear anywhere except through  $s$ , and  $u$ ,  $v$ ,  $K$ ,  $\tau$  and  $\zeta$  were all *separable*, that is, each could be expressed as the product of a function of  $x$  and a function of  $s$ . In view of this, we expect that the 2D plume model given by Eq. (4.2) will take a simpler form if we change the independent variables from  $x$  and  $y$  to  $x$  and  $s$ . This is a straightforward procedure that involves the chain rule; for more information, see Zwillinger (1989, p. 109). This change of variables is given by the transformation  $\eta(x, y) = x$ ,  $s(x, y) = \sigma y/x$ , which is easily inverted to get  $x(\eta, s) = \eta$ ,  $y(\eta, s) = \eta s/\sigma$ . From the chain rule then, we have

$$I_s = I_x x_s + I_y y_s = I_y \left(\frac{\eta}{\sigma}\right) \quad (4.5)$$

$$I_\eta = I_x x_\eta + I_y y_\eta = I_x + I_y \left(\frac{s}{\sigma}\right). \quad (4.6)$$

Solving for  $I_x$  and  $I_y$ , we have

$$I_x = I_\eta - \left(\frac{s}{\eta}\right) I_s \quad (4.7)$$

$$I_y = \left(\frac{\sigma}{\eta}\right) I_s. \quad (4.8)$$

Another application of the chain rule yields

$$I_{yy} = \left(\frac{\sigma}{\eta}\right)^2 I_{ss}. \quad (4.9)$$

Inserting the last three expressions into (4.2) and simplifying we find that

$$2\eta \left[ F'(s) I_\eta + \frac{\lambda I}{u_c(\eta)} \right] = F I_s - \left[ \left( \frac{FF'}{F''} \right) I_s \right]_s. \quad (4.10)$$

However, using the product-rule to write

$$\left[ F' \left( \frac{F I_s}{F''} \right) \right]_s = F I_s + F' \left( \frac{F I_s}{F''} \right)_s \quad (4.11)$$

and recalling that  $\eta = x$  and  $u_c(x) = \sqrt{x_a/x}$ , Eq. (4.11) can be further simplified to

$$I_x = - \left[ \frac{\lambda_a x^{1/2}}{F'(s)} \right] I - \frac{1}{2x} \left[ \left( \frac{F(s)}{F''(s)} \right) I_s \right]_s. \quad (4.12)$$

Here, the shorthand  $\lambda_a = \lambda/\sqrt{x_a}$  has been introduced to simplify this and subsequent expressions. This new PDE in independent variables  $x$  and  $s$  expresses the fact that the inventory,  $I$ , decreases as we move offshore due to both the vertical loss of sediment (as it is deposited on the seafloor) and the lateral spread of sediment between lines of constant  $s$  due to turbulent diffusion and advection by  $v$ . Note that  $F(s)$  will be a known function once a particular 2D turbulent jet solution has been selected (e.g.  $F(s) = \tanh(s)$  for the Goertler solution), so this equation is much simpler than the original Eq. (4.2). This PDE is parabolic and linear in the dependent variable,  $I$ , but has nonconstant coefficients. Were it not for the nonconstant coefficients, solutions could be found by standard methods such as separation of variables and Laplace and Fourier transforms. One can think of the  $x$ -axis as a time axis, such that any initial distribution of sediment near the river mouth,  $I(0, y)$ , can be expected to “evolve” toward a smooth *similarity solution*, as is typical of many parabolic PDEs. However, our goal here is not to solve the general initial-value problem but rather to find the solution for  $I(x, s)$  that corresponds to the outer zone similarity solutions that we have for  $u, v$  and  $K$ .

Eq. (4.12) has no nontrivial solution of the separable form  $I = A(x)B(s)$  or  $I = \exp[A(x)B(s)]$ . It also appears that there is no similarity variable  $r(x, s)$  such that (4.12) can be reduced to an ODE of the form  $A(r)H''(r) + B(r)H'(r) + C(r)H(r) = 0$ . It

can also be shown that there are no functions  $A(x, s)$  and  $B(x, s)$  such that changing the dependent variable to  $J = AI$  allows Eq. (4.12) to be written in the simpler form  $J_{ss} = BJ_x$ . Eq. (4.12) has a form that is somewhat similar to the well-known Black–Scholes PDE (Black and Scholes, 1973) that arises in the pricing of stock options.

#### 4.3. Special case solutions to the 2D plume model

While a closed-form similarity solution to (4.12) is so far unavailable, it is possible to obtain solutions for several special cases that correspond to dropping terms in (4.12). It is instructive to examine these solutions as they provide clues in the form of a general similarity solution.

*Case 1.* For the special case of  $\lambda = 0$  there is no vertical loss of sediment and Eq. (4.12) has the solution

$$I(x, s) = cu(x, s) = cu_c(x)F'(s), \tag{4.13}$$

where  $c$  is an arbitrary constant. As noted previously, the equation for the sediment inventory becomes identical to the momentum equation for the 2D turbulent jet in this case, but has a different initial value at  $x = x_a$ .

*Case 2.* If we drop the last term in Eq. (4.12) altogether, which corresponds to dropping both the  $v$ -term and  $K$ -term in Eq. (4.2), then the

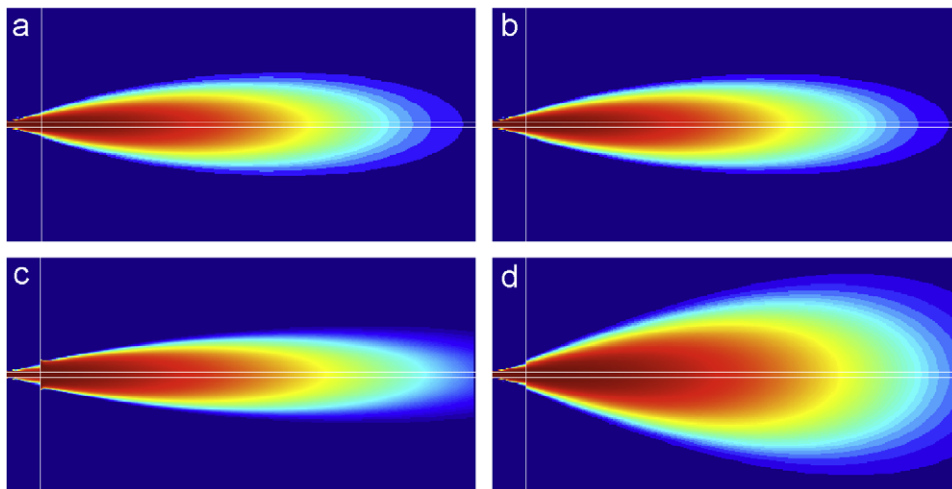


Fig. 8. Approximations to  $I(x, y)$  using  $u, v$  and  $K$  from Albertson’s 2D jet model. (a) Numerical solution to surficial plume equation for  $u_0 = 1$  m/s,  $b_0 = 500$  m,  $\lambda = 6$  1/day (medium silt) and nondimensional  $\lambda = 0.035$  (upper left). (b) “Close approximation” given in Section 4.6 (upper right). (c) Approximate solution from Case 2 (lower left). (d) Approximate solution from Case 3 (lower right). A white vertical line shows boundary between inner and outer zones and white horizontal lines extend from edges of river mouth. Here  $x_a = 5.13$ ,  $\sigma = 6.43$  and each image spans 70 river widths.

solution is (Fig. 8c)

$$I(x, s) = c \exp \left[ -\frac{2 \lambda_a x^{3/2}}{3 F'(s)} \right]. \tag{4.14}$$

Case 3. If the  $\lambda$  term in (4.12) did not contain  $F'(s)$  in the denominator, then the solution would be (Fig. 8d)

$$I(x, s) = c u(x, s) \exp[-\frac{2}{3} \lambda_a x^{3/2}] \tag{4.15}$$

which reduces to  $I(x, s) = c u(x, s)$  as it should when  $\lambda = 0$ .

Case 4. For the special case  $K = 0$ , there is no turbulent diffusion and the advective transport terms exactly balance the sediment loss term. The simplified form of the surficial plume model is then

$$I_x = \frac{F(s)}{F'(s)} \frac{I_s}{2x} - \frac{\lambda_a x^{1/2} I}{F'(s)}. \tag{4.16}$$

A solution for this case is given by

$$I(x, s) = \{a_1 \ln[F(s)x^{1/2}] + a_2\} \exp[L(x, s)] \tag{4.17}$$

$$L(x, s) = 2\lambda_a x^{3/2} F^3(s) \left\{ a_3 + \int_{t=1}^s [F(t)]^{-4} dt \right\}. \tag{4.18}$$

Here  $a_1$ ,  $a_2$  and  $a_3$  are arbitrary integration constants. If  $F(0) = 0$ , as it does for the Goertler and Albertson solutions, then we must set  $a_1 = 0$  so that the solution doesn't diverge on the centerline. It can then be shown for this solution that

$$I(x, 0) = a_2 \exp[-\frac{2}{3} \lambda_a x^{3/2}], \tag{4.19}$$

as it must, since  $v = 0$ ,  $I_s = 0$  and  $F'(0) = 1$  on the centerline. For the Goertler case where  $F(s) = \tanh(s)$ , the  $s$ -dependent part of  $L(x, s)$  can be simplified to  $s \tanh^3(s) - \tanh^2(s) - \frac{1}{3}$  and equals  $-\frac{1}{3}$  for  $s = 0$ .

Case 5. If we expand the last term in (4.12), then we get an  $I_s$  term and an  $I_{ss}$  term. If we change the dependent variable to  $H$  via  $I(x, s) = I_a \exp(H(x, s))$ , and define  $G(x, s) = I_{ss}/I$ , the resulting first-order equation can be solved for a general function,  $G$ , to get

$$\begin{aligned} H(x, s) = & -2\lambda_a x^{3/2} \int_{t=1}^s A(t)C(t) L(t, s)^{3/2} dt \\ & - \int_{t=1}^s B(t)C(t)G[xL(t, s), t] dt \\ & + a_1 [J(s) - \frac{1}{2} \ln(x)]. \end{aligned} \tag{4.20}$$

Here  $A(s) = 1/F'(s)$ ,  $B(s) = F(s)/F''(s)$ ,  $C(s) = 1/B'(s)$ ,  $J(s) = \int_{t=1}^s C(t) dt$ ,  $M(s) = \exp[2J(s)]$ ,

$L(t, s) = M(t)/M(s)$  and  $a_1$  is an arbitrary constant. Letting the first integral in (4.20) be  $P(s)$ , L'Hôpital's rule and the fact that  $C(s) = J'(s)$  can be used to show that  $P(0) = \frac{1}{3}$  and  $P'(0) = 0$ , for any  $F(s)$  as long as  $F'(0) = 1$ . If the equation  $G = H_{ss} + H_s^2$  could be solved for  $G$ , then this would provide a solution to (4.12). It is clear that  $G$  must depend on  $\lambda$ , and  $c_1$  could also in a particular solution. The case where  $G = 0$  provides a solution to the special case where (4.12) is expanded and the  $I_{ss}$  term is dropped.

#### 4.4. A regular perturbation solution to the 2D plume model

The *regular perturbation method* is an analytical method that can sometimes be used to find approximate solutions to differential equations that have a small parameter in one of the lower-order terms (Zwillinger, 1989, p. 473). Notice that if  $\lambda_a$  is small, then (4.12) is of this form. Since  $I \geq 0$ , we lose no generality by searching for a solution of the form  $I = e^H$ , where  $H = H(x, s)$ . Inserting this into (4.12) and simplifying we find that  $H$  must satisfy the equation

$$-2xH_x = 2\lambda_a x^{3/2} A(s) + B'(s)H_s + B(s)(H_{ss} + H_s^2). \tag{4.21}$$

Here,  $A(s) = 1/F'(s)$  and  $B(s) = F(s)/F''(s)$  have been used to simplify the notation. The idea of the regular perturbation method is to assume that the solution can be expanded in powers of  $\lambda_a$  as

$$H = \sum_{k=0}^{\infty} \lambda_a^k H_k(x, s). \tag{4.22}$$

Eq. (4.22) is then inserted into (4.21) and it is assumed that all resulting terms with the same power of  $\lambda_a$  must add to zero. This results in the following sequence of PDEs

$$-2x(H_0)_x = B'(H_0)_s + B[(H_0)_{ss} + (H_0)_s^2] \tag{4.23}$$

$$\begin{aligned} -2x(H_1)_x = & B'(H_1)_s + B[(H_1)_{ss} + 2(H_0)_s(H_1)_s] \\ & + 2x^{3/2} A(s) \end{aligned} \tag{4.24}$$

$$-2x(H_2)_x = B'(H_2)_s + B[(H_2)_{ss} + 2(H_0)_s(H_2)_s + (H_1)_s^2] \tag{4.25}$$

$$-2x(H_k)_x = B'(H_k)_s + B[(H_k)_{ss} + 2(H_0)_s(H_k)_s + R_k]. \tag{4.26}$$

Here  $R_k(x, s)$  is a sum of terms of the form  $c(H_i)_s (H_j)_s$ , such that  $(i + j) = k$ . If  $i = j = k/2$ ,

then  $c = 1$ , otherwise  $c = 2$ . Therefore, lower-order solutions must be found before the PDEs for higher-order solutions can be completely specified. As long as  $\lambda_a$  is sufficiently small, we expect that higher-order terms in (4.22) will provide ever-smaller contributions to the approximate solution. Notice that (4.23) corresponds to (4.12) with  $I = e^H$  and  $\lambda_a = 0$ . As seen in Case 1 of the last section, its solution is therefore  $H_0 = \ln(cu)$ , or

$$H_0(x, s) = \ln[F'(s)] - \frac{1}{2} \ln(x) + c. \quad (4.27)$$

It can be shown that Eq. (4.24) has the separable solution

$$H_1(x, s) = -\frac{x^{3/2}}{F'(s)}, \quad (4.28)$$

and this satisfies the boundary condition that  $I(x, s)$  goes to zero as  $s$  goes to infinity. It can also be shown that if we seek separable solutions to (4.25) and (4.26) of the form  $H_k = x^{3k/2} G_k(s)$ , then they reduce to an ODE for  $G_k(s)$ . Unfortunately, solutions for  $G_k(s)$  when  $k > 1$  have not yet been found. The final form of the perturbation solution is then

$$I(x, s) = \frac{cF'(s)}{\sqrt{x}} \exp \left[ -\frac{\lambda_a x^{3/2}}{F'(s)} + \sum_{k=2}^{\infty} \lambda_a^k x^{3k/2} G_k(s) \right]. \quad (4.29)$$

Based on the similarity between the first-order solution and Case 3 (see Fig. 8d), it is expected that the second-order solution may provide a good approximate solution to (4.12) if  $G_2(s)$  can be found.

#### 4.5. A numerical solution to the 2D plume model

Following the basic approach described by Syvitski et al. (1998), the 2D plume model in the form of Eq. (4.2) can be solved numerically. With the plume centerline extending seaward along the  $x$ -axis, and with a square-pulse initial profile at  $x = 0$  such that  $I(0, y) = 1$  for  $y \in [-1/2, 1/2]$ , the solution is determined by iterating column by column from left to right across the domain. The numerical scheme is second-order accurate in  $y$  and first-order accurate in  $x$  and uses a tridiagonal matrix solver such as the one given by Press et al. (1990, p. 47). Closed-form expressions for  $u$ ,  $v$  and  $K$  are used, from either the Albertson or Goertler 2D jet model. The resulting solution for the case of (nondimensional)  $\lambda = 0.035$  is shown in Fig. 8a. All of the subroutines used to numerically solve (4.2) and

create the images in this paper are available as interactive data language (IDL) source code at <http://www.iamg.org/CGEditor>.

One method for examining the integrity of the numerical solution method is to compute *residuals*. The idea is to numerically evaluate each term in the surficial plume equation for the numerical solution and then compute the difference between the left- and right-hand sides of the equation for every grid cell in the domain. For a perfect solution the result would be zero for every grid cell. For our numerical solution all of the residuals fall between  $-0.023$  and  $0.0061$ . For comparison, if we start with the Albertson 2D jet solutions for  $u$ ,  $v$  and  $K$  and compute the residuals of the  $x$ -momentum equation, they all fall between  $-0.0029$  and  $0.0012$ .

#### 4.6. An approximate solution to the 2D plume model

Although a closed-form solution to the surficial plume model is not yet available, the following expression for  $I(x, s)$  provides a fairly close approximation to the numerical solution for  $\lambda = 0.035$ :

$$I(x, s) = I_a e^{-(m_1 s)^2} \left( \frac{x_a}{x} \right)^p \exp[-(2/3)b\lambda_a x^{3/2} e^{(m_2 s)^2}] \quad (4.30)$$

where  $m_1 = 1.2$ ,  $m_2 = 0.6$ ,  $p = 0.8$  and  $b = 0.9$ . These four constants can be adjusted to give a closer fit for other values of  $\lambda$ . The constant  $I_a$  is determined by matching the inner zone solution on the centerline at  $x = x_a$ , and is given by

$$I_a = \exp(-\lambda x_a) / I(x_a, 0). \quad (4.31)$$

This approximation may be accurate enough for many applications, in which case a numerical approach to the solving the 2D plume equation would be unnecessary. See Fig. 8b. In fact, it turns out that the residuals for this approximation fall between  $-0.01836$  and  $2.695e-7$  and therefore span a narrower range than the residuals of the numerical solution discussed in Section 4.5.

#### 4.7. Approximations to the centerline inventory

The method of assigning SSC values to pixels in satellite images to be introduced in Section 5 requires a knowledge of  $I(x, 0)$ , the inventory on the centerline of a 2D sediment plume. While an analytic solution to the governing equations is not yet available, it is possible to derive some results regarding the centerline inventory, including upper bounds and a close



approximation. Two such results are given here and two more can be found in Appendix A.

4.7.1. Upper bounds for the centerline inventory

As shown in previous sections, the decrease in sediment inventory along the centerline of a plume is due to three different effects: (1) the vertical loss due to settling, (2) advective transport away from the centerline by the  $v$ -component of velocity and (3) diffusive transport away from the centerline by turbulence. In the alternate version of the plume model, (4.12), the second two effects were combined into a single term. Since there must be a greater decrease in the centerline inventory with both effects operating than with either effect acting alone, we can use special-case solutions to provide upper bounds to  $I(x, 0)$ . The special-case solutions from Cases 1 and 2 of Section 4.3 are

$$I_1(x, s) = c_1 u(x, s) = c_1 u_c(x) F'(s) \tag{4.32}$$

$$I_2(x, s) = c_2 \exp \left[ -\frac{2}{3} \frac{\lambda_a x^{3/2}}{F'(s)} \right] \tag{4.33}$$

where

$$c_1 = \exp(-\lambda x_a) \tag{4.34}$$

$$c_2 = \exp(-\lambda x_a) \exp \left[ \left( \frac{2}{3} \right) \lambda_a x^{3/2} \right], \tag{4.35}$$

as required so that  $I(x_a, 0) = \exp(-\lambda x_a)$ . Since both  $I_1$  and  $I_2$  provide upper bounds on the centerline, we must have

$$I(x, 0) \leq \min\{I_1(x, 0), I_2(x, 0)\}. \tag{4.36}$$

Fig. 9 shows the curves,  $I_1(x, 0)$ ,  $I_2(x, 0)$  and  $I_1(x, 0)I_2(x, 0)$  for the case of  $\lambda = 0.035$ . It is seen that  $I_1(x, 0)$  provides a tighter upper bound for  $x < x_c$  and  $I_2(x, 0)$  provides a tighter bound for  $x > x_c$ , where  $x_c \approx 17$  river widths. The product of  $I_1$  and  $I_2$  is an example of a function that is lower than both  $I_1$  and  $I_2$  since both are always less than 1.

4.7.2. A close approximation for the centerline inventory

If the 2D plume model is solved numerically using the Albertson 2D jet model for  $u$ ,  $v$  and  $K$  as in Section 4.5, the resulting centerline profile can then be compared to various approximations. Doing so, we find that

$$I(x, 0) = c_2 \left( \frac{x_a}{x} \right)^{p(\lambda)} \exp \left[ -\left( \frac{2}{3} \right) \lambda_a x^{3/2} \right], \tag{4.37}$$

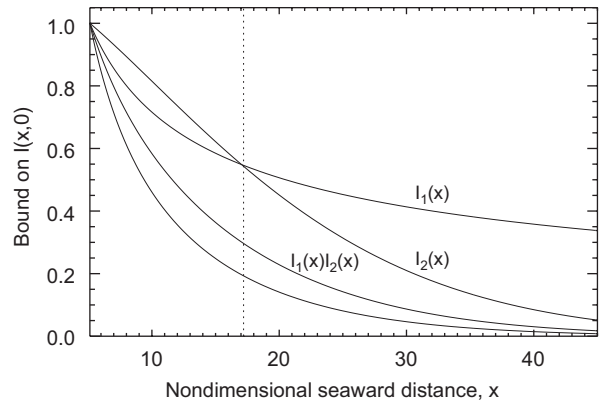


Fig. 9. Upper bounds for the centerline inventory,  $I(x, 0)$ . Top two curves are plots of  $I_1(x, 0)$  and  $I_2(x, 0)$ , given by setting  $s = 0$  in (4.22) and (4.23). Product of top two curves gives a curve that always lies below each of them, but above bottom curve, which is numerical solution. See also Fig. 10.

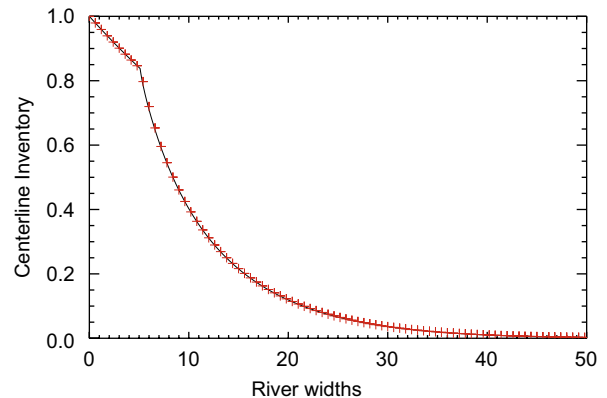


Fig. 10. A close approximation to  $I(x, 0)$ . Black curve shows numerical solution with  $u$ ,  $v$  and  $K$  from Albertson’s 2D jet model ( $\lambda = 0.035$  and  $x_a = 5.13$ ). Plus signs in outer zone show approximation given by (4.27), with  $p = 0.84$ , while for inner zone they show Eq. (4.4).

provides a very close approximation to the centerline inventory, where  $p(\lambda)$  is chosen to provide the best fit and is typically between 0.75 and 1. If  $p(\lambda) \geq \frac{1}{2}$ , then this approximation honors the upper bounds of the last section. The constant,  $c_2$ , is the same as given in Eq. (4.35). Fig. 10 compares this approximation to the numerical solution for the case of (nondimensional)  $\lambda = 0.035$ .

4.8. Centerline inventory for a mixture of grainsizes

When SSC is measured *in situ*, it is generally the total SSC that is reported (see Syvitski et al., 1985). So it is of interest to know how results for individual

grainsizes can be aggregated. Given the *dimensional* inventory for each grainsize at the river mouth, we can compute the (nondimensional) total centerline inventory at all distances  $x$  from the mouth as follows. In the case of a discrete mixture of  $n$  grainsizes, we first compute the fraction that each grainsize contributes to the total inventory at the mouth as

$$f_k = \frac{I_k}{\sum_{k=1}^n I_k} \tag{4.38}$$

and then we compute

$$I_{tot}(x) = \sum_{k=1}^n f_k I[x, 0; \lambda(D_k)] \tag{4.39}$$

where  $D_k$  is the grainsize of a particular component material and  $I(0, 0; \lambda) = 1$  for all values of  $\lambda$ . For the case of a continuous mixture of grainsizes, we have

$$I_{tot}(x) = \int_{D=0}^{\infty} f(D) I[x, 0; \lambda(D)] dD \tag{4.40}$$

where now  $f(D)$  is a function that integrates to one that describes the initial distribution of inventories as a function of grainsize,  $D$ , at the river mouth. Here again,  $I$  is the nondimensional inventory so that  $I(0, 0; \lambda) = 1$ . As an example, suppose that the initial mixture of inventories follows an exponential distribution,  $f(D) = a \exp(-aD)$ , which implies that the mean grainsize is  $(1/a)$ . Recall from Eq. (4.3) that the *dimensional* removal rate constant is seen to vary linearly with grainsize as  $\lambda'(D) = mD + b$ , where  $m = 0.222$ ,  $b = 1.573$ ,  $D$  is measured in microns and the units are 1/day. Before using it here, it must first be made nondimensional by multiplying by  $b_0/(86400u_0)$  (see (3.6)). If we use the close approximation for  $I(x, 0)$  from Section 4.7, but assume for simplicity that  $p(\lambda) = p$  is a constant, the integral (4.40) can be computed to get

$$I_{tot}(x) = I_a \left(\frac{x_a}{x}\right)^p \left(1 + \frac{2mx^{3/2}}{3a\sqrt{x_a}}\right)^{-1} \exp\left(-\frac{2}{3} \frac{bx^{3/2}}{\sqrt{x_a}}\right). \tag{4.41}$$

Here again,  $I_a$  is a constant that is chosen such that the inventory equals 1 at  $x = x_a$ . Based on the results of Section 4.7, we expect that  $p \in (0.5, 1)$ . This equation can be plotted as a function of  $x$  for the empirical values of  $m$  and  $b$  and for different values of  $a$  (see Fig. 11). Since typical grainsizes are between about 1 and 100 $\mu\text{m}$ , we expect that  $a \in (0.01, 1)$ . Fig. 11 shows that if the mean grain

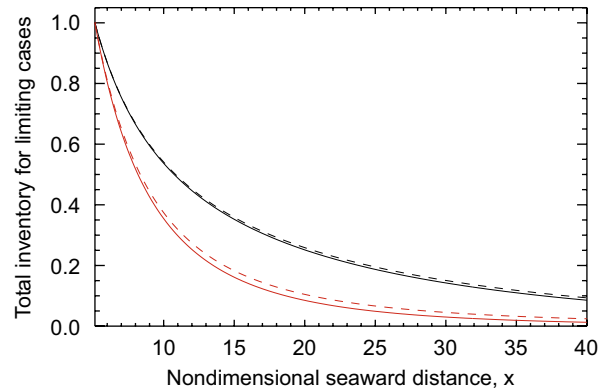


Fig. 11. Centerline inventory for an exponential mixture of grainsizes. Solid curves show limiting cases where the mean grainsize is 1  $\mu\text{m}$  (top), and 100  $\mu\text{m}$  (bottom). Top dashed curve shows result of dropping middle term from (4.41) and bottom dashed curve shows result of dropping exponential term.

size at the mouth is small, then the exponential term in (4.41) will dominate the middle term and the centerline inventory will have more of an exponential falloff. If the mean grain size is large, however, then the middle term will dominate the exponential term and the centerline inventory for the mixture will have more of a power-law falloff.

## 5. A new method for deriving SSC from a satellite image

### 5.1. Centerline inventory as a transfer function

As discussed in Section 2, there are a variety of different methods for collapsing the information contained in multi-band satellite imagery to create images that show *relative SSC*. Such an image can be used to compare any two pixels and determine which has a higher SSC value, but does not provide a definite value in real units such as  $\text{kg}/\text{m}^3$ . In order to assign a real SSC value to each pixel in a satellite image, we therefore need a *transfer function* that maps every relative SSC value to its corresponding real value. Making “ground truth” measurements of SSC at various locations within an image is clearly one way to develop a transfer function, but this is costly and difficult and unlikely to be portable from one setting to another. Analyzing different sediment–water mixtures in a laboratory setting is another way, and has produced promising results. However, the results presented in previous sections suggest that there is an entirely different way to approach this problem.

Expressions such as (4.37) or (4.41) allow us to predict the inventory as a function of distance along the centerline of a time-averaged sediment plume. Since the depth of a buoyant 2D plume is approximately constant and equal to the river depth at the mouth, Eq. (4.1) can be used to compute SSC from inventory. Note that SSC varies continuously between its highest and lowest possible values along the plume centerline. It follows that if we develop a transfer function for the pixels on the centerline, then that transfer function will allow us to assign an SSC value to every pixel in the image. That is, since every inventory value in the image occurs somewhere along the centerline, we can create a lookup table for converting relative SSC values to absolute SSC values from the theoretical (absolute) and observed (relative) centerline values. The plume centerline does not need to be a straight line, since it is expected based on results for deflected plumes (see Section 3.7 and Appendix B) that there will be little, if any, geometric stretching along the centerline as a result of its deflection. Note from (3.40) that the shear stress on the centerline is zero, which is fundamental to the integrity of the jet; stretching would seem to require a nonzero shear stress on the centerline. The variable  $x$  in the equations is simply replaced by distance measured along the centerline of the largest jet in the image. This idea is best illustrated by referring back to Fig. 1, which shows a time-averaged AVHRR

image of relative SSC values near the Mississippi River delta. Notice that there is one main jet (Southwest Pass) and several smaller jets, and that the overall geometry is much more complex than the geometry of a single symmetric jet.

Note that once we have determined the transfer function by this method, it can be re-used to assign SSC values in future satellite images of the same region, assuming that the river discharges similar materials in similar proportions during future events of interest. However, there are several reasons that the image used to derive the transfer function should correspond to the largest possible flood event. First, it is best if the discharge at the river mouth remains approximately constant over the period of time for which images will be averaged, and discharge varies less rapidly during a large event. (This also allows for more images, since the return frequency of the satellite is likely fixed.) Second, since radiation stresses due to incoming waves were not included in the derivation of the centerline results, the strength of the jet should be as large as possible as compared to the strength of the waves. (Note that it may be possible to model the effect of the radiation stresses via inclusion of the pressure gradient term in (3.1).) Finally, the dynamic range of SSC values during a flood event will be larger, resulting in a greater signal to noise ratio.

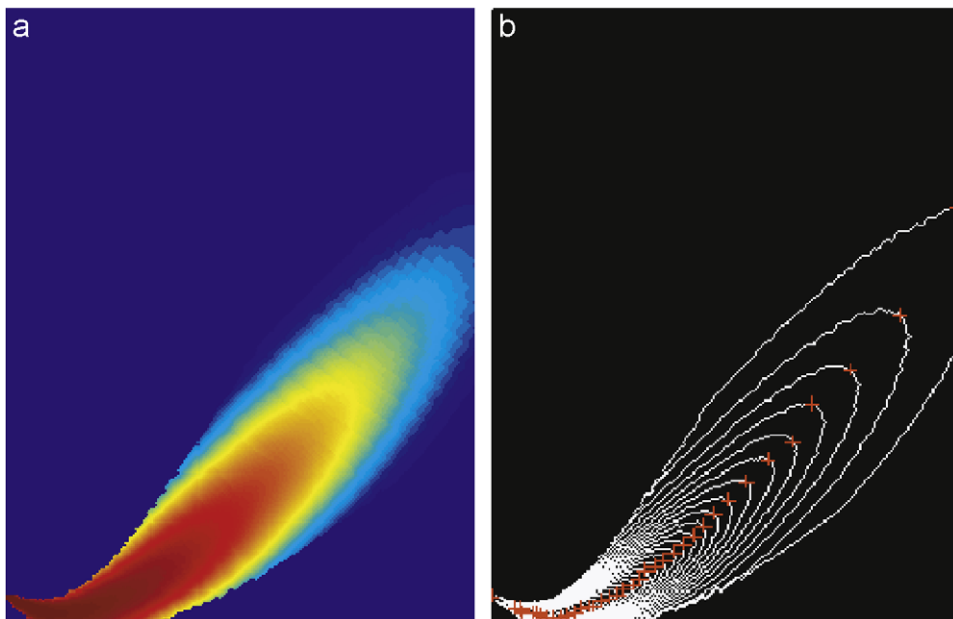


Fig. 12. (a) A simulated plume, with a deflected centerline. (b) Results of applying a curvature-based algorithm for finding pixels on contour curves that lie on centerline. Red plus signs indicate points of maximum curvature.

## 5.2. Finding the pixels on the centerline of the plume

In order to apply the methodology of the last section, a robust method is required for identifying the image pixels that lie on the plume centerline. Fig. 12 shows the results of a computer program written by the author for this purpose. An image of relative SSC values is first contoured, and then each contour is traced to find the point on the curve where the curvature is maximum and of the correct sign. Linear interpolation between these points of maximum curvature is then used to return continuous coordinates of pixels that lie on the plume centerline. These pixel coordinates and the distance along the centerline from the mouth to each pixel are used together with a closed-form expression for  $I(x, 0)$  to create a lookup table that converts relative SSC values to actual SSC values. This lookup table can then be applied to all image pixels to create a map of actual SSC values. When this was done for test images of simulated time-averaged plumes, it was possible to reconstruct the original grid of SSC values using this procedure.

## 6. Conclusions

The results presented here provide a mathematical framework for the modeling and further study of sediment plumes produced at river mouths. Known similarity solutions for 2D turbulent jets were discussed and shown to be special cases of a more general jet model in which  $u$ ,  $v$ ,  $K$ ,  $\tau$  and  $\zeta$  can all be given in closed-form in terms of a single function,  $F(s)$ , and its derivatives. In addition, an approximate method for computing how the centerline of a turbulent jet is deflected by the Coriolis effect was presented. An alternate form of the advection–diffusion–deposition equation that governs sediment plumes was also given in terms of  $F(s)$ , and several special-case solutions were presented. A similarity solution for the inventory,  $I(x, y)$ , was found numerically and compared to several special-case solutions and bounds. A closed-form approximation that provides a very close match to the numerical solution for  $I(x, y)$  was also given. A variety of results for the centerline inventory,  $I(x, 0)$ , were given, including upper bounds and a close approximation. Well-documented source code for numerically finding a similarity solution to the 2D plume equation and for generating all of the figures in this paper is available at: <http://www.iamg.org/CGEditor>.

This paper introduces a new method for estimating suspended sediment concentrations and deposition rates from remotely sensed images that is based on mathematical models for 2D turbulent jets and sediment plumes. This method offers several advantages over existing methods, including a strong foundation in hydrodynamics, greater portability, ease of implementation and the time required to obtain a result. It also requires a relatively small amount of input data that is expected to be much easier to obtain (since it can all be collected at the river mouth) than the data required by other methods. Note that once the transfer function has been determined for a given river, it is expected that the same transfer function can be used to derive SSC values from satellite images that are subsequently obtained for the same area with the same sensor. However, while the results presented here provide a complete theoretical framework and a proof of concept, additional work is required to validate the method in an operational setting and to compare results to those obtained by existing methods. It is likely that optimal results will be obtained by using this method in conjunction with existing spectral methods. For example, an SSC image created by another method could be used as the input image to the current method as a check on whether the values from the other method are reasonable from a hydrodynamic point of view. These issues will be explored in future work.

## Appendix A. Other results for the centerline inventory

### A.1. Use of integral equations

A line of reasoning similar to what was used in Section 3.3 to obtain an expression for  $u(x, 0)$  can be used to seek an expression for  $I(x, 0)$ . We first write the 2D plume model (4.2) in conservative form by adding the product of  $I$  and the continuity equation (3.2), which yields

$$(uI)_x + (vI)_y + \lambda I = (KI_y)_y. \quad (\text{A.1})$$

Integrating each term in this equation from  $y = -\infty$  to  $\infty$ , the  $y$ -derivative terms drop out (since  $I$  and  $I_y$  decrease to zero as  $|y| \rightarrow \infty$ ) and we find that

$$\int_{y=-\infty}^{\infty} (uI)_x dy = \int_{y=-\infty}^{\infty} -\lambda I dy. \quad (\text{A.2})$$

Note that the total flux of sediment across a line of constant  $x$  is given by

$$Q(x) = \int_{y=-\infty}^{\infty} uI \, dy = \frac{xu_c(x)}{\sigma} \int_{s=-\infty}^{\infty} F'(s)I(x, s) \, ds. \tag{A.3}$$

The second expression for  $Q$  follows by changing variables in the integral from  $y$  to  $s$  and using the fact that  $u = u_c(x)F'(s)$ . The derivative with respect to  $x$  can be moved outside of the first integral in (A.2). If we define

$$G(x) = \int_{s=-\infty}^{\infty} I(x, s) \, ds \tag{A.4}$$

$$H(x) = \int_{s=-\infty}^{\infty} F'(s)I(x, s) \, ds \tag{A.5}$$

then Eq. (A.2) can be written as

$$[x^{1/2}H(x)]_x = -\lambda_a x G(x). \tag{A.6}$$

Recall that we were able to solve (3.9)—an integral equation similar to (A.2)—for  $u_c(x) = u(x, 0)$  by assuming that  $u$  had the separable form  $u(x, s) = u_c(x)F'(s)$ . We can try to use the same idea here by assuming that  $I(x, s) = A(x)B(s)$  and  $A(x) = I(x, 0)$ . This implies that  $G(x) = c_1A(x)$  and  $H(x) = c_2A(x)$ . Eq. (A.6) is then easily solved for  $A(x)$  to find that

$$I(x, 0) = \frac{c_3}{\sqrt{x}} \exp\left[-\frac{2c_1}{3c_2} \lambda_a x^{3/2}\right] \tag{A.7}$$

where

$$c_1 = \int_{s=-\infty}^{\infty} B(s) \, ds \tag{A.8}$$

$$c_2 = \int_{s=-\infty}^{\infty} F'(s)B(s) \, ds. \tag{A.9}$$

This expression for  $I(x, 0)$  reduces to  $u_c(x)$  in the case where  $\lambda = 0$ , as it should. However, it can be shown that the surficial plume model does not have a solution of the form  $I = A(x)B(s)$ , so Eq. (A.7) only provides a rough approximation to the centerline inventory,  $I(x, 0)$ . (See Fig. 8.) Recall that we are working with nondimensional equations, so we can assume without loss of generality that  $A(x_a) = 1$  and  $B(0) = 1$  and then solve for  $c_3$ .

### A.2. Assuming that $I_{ss}(x, 0)$ is Known

If we insert  $s = 0$  into Eq. (4.12), recall that  $F'(0) = 1$  and define

$$H(x) = I(x, 0) \tag{A.10}$$

$$g(x) = I_{ss}(x, 0)/I(x, 0) \tag{A.11}$$

$$c_0 = \lim_{s \rightarrow \infty} \left\{ \frac{F(s)}{F''(s)} \right\} \tag{A.12}$$

then we get the following ODE for the inventory on the plume centerline

$$H'(x) = -H(x) \left[ \lambda_a x^{1/2} - \frac{c_0 g(x)}{2x} \right]. \tag{A.13}$$

The only trouble is that we don't know  $g(x)$ . However, Eq. (A.13) can be solved for a general function  $g(x)$  to get

$$H(x) = c_1 \exp \left[ -\left(\frac{2}{3}\right) \lambda_a x^{3/2} - \left(\frac{c_0}{2}\right) \int_{t=x_a}^x \frac{g(t)}{t} \, dt \right]. \tag{A.14}$$

Here  $c_1$  is a constant that can be used to satisfy the initial condition at the zone boundary. The constant  $c_0 < 0$  and equals  $-\frac{1}{2}$  for both the Goertler and Albertson solutions. An approximate form for  $g(x)$  could be determined from a numerical solution and then used in this equation to get an approximate expression for the centerline inventory. Note that  $g(x) < 0$  because  $I(x, 0) > 0$  and  $I_{ss}(x, 0) < 0$  represents the curvature at  $s = 0$  for a cross-section of  $I$  that is perpendicular to the centerline. Our close approximation result from Section 4.6 suggests that  $g(x) \approx c_2$ , where  $c_2 < 0$  is a constant that depends on  $\lambda$ .

### Appendix B. A 2D turbulent jet in cross-flow

The results presented in this paper assume that the river jet enters a quiescent ocean at right angles to the coastline. However, some results are also available for jets discharging at an angle into a cross-flow of uniform velocity. In the current context, this corresponds to the case where there is a longshore current of velocity  $u_1$  and an arbitrary ocean entrance angle. Let  $\theta_0 \in (-\pi/2, \pi/2)$  be the ocean entrance angle as measured counter-clockwise from the  $x$ -axis (the centerline of the nondeflected jet). Recall that  $u_0$  and  $b_0$  are the velocity and width at the river mouth and let  $\alpha = u_0/u_1$  be the



dimensionless ratio of velocities. Abramovich (1963) (see also Rajaratnam, 1976, p. 205) derived a nondimensional equation for the deflected centerline of the 2D turbulent jet as a parabola

$$y_c = \pm x_c [x_c B(\theta_0)/4 - \tan(\theta_0)] \quad (\text{B.1})$$

where  $B(\theta_0) = C_d/(2b_0 \alpha^2 \cos(\theta_0))$  and  $C_d \approx 2.0$ . The sign in (B.1) is given by the sign of  $u_1$ . This is the Abramovich result in terms of the coordinate system used in this paper. Notice that unlike the Coriolis effect, cross-flow cannot cause the centerline of a plume to curve back toward the shore.

## References

- Abramovich, G., 1963. *The Theory of Turbulent Jets*. MIT Press, MA, 671 pp.
- Albertson, M., Dai, Y., Jensen, R., Rouse, H., 1950. Diffusion of submerged jets. *American Society of Civil Engineers Transactions* 115, 639–697.
- Amos, C., Alfoldi, T., 1979. The determination of SSC in a macro tidal system using Landsat data. *Journal of Sedimentary Petrology* 49, 159–174.
- Amos, C., Topliss, B., 1985. Discrimination of suspended particulate matter in the bay of Fundy using the Nimbus-7 coastal zone color scanner. *Canadian Journal of Remote Sensing* 11 (1), 85–92.
- Batchelor, G., 1988. *An Introduction to Fluid Dynamics*. Cambridge University Press, Cambridge, 615 pp.
- Black, F., Scholes, M., 1973. The pricing of options and corporate liabilities. *Journal of Political Economy* 81 (3), 637–654.
- Bursik, M., 1995. Theory of the sedimentation of suspended particles from fluvial plumes. *Sedimentology* 42, 831–838.
- Durrant, D., 1993. Is the Coriolis force really responsible for the inertial oscillation? *Bulletin of the American Meteorological Society* 74, 2179–2184.
- Fong, D., Geyer, W., 2002. The alongshore transport of freshwater in a surface-trapped river plume. *Journal of Physical Oceanography* 32, 957–972.
- Goertler, H., 1942. Berechnung von aufgaben der freien turbulenz auf grund eines neuen naherungsansatzes (Calculating problems concerning free turbulence based on a new approximation formula). *Zeitschrift fur Angewandte Mathematik und Mechanik* 22, 244–254.
- Gordon, H., Brown, O., Jacobs, M., 1975. Computed relationships between the inherent and apparent optical properties of a flat homogeneous ocean. *Applied Optics* 14, 417–427.
- Hitchcock, G., Wiseman Jr., W., Boicourt, W., Mariano, A., Walker, N., Nelsen, T., Ryan, E., 1997. Property fields in an effluent plume of the Mississippi River. *Journal of Marine Systems* 12, 109–126.
- McIntyre, D., 2000. Using great circles to understand motion on a rotating sphere. *American Journal of Physics* 68 (12), 1097–1105.
- Mertes, L., Smith, M., Adams, J., 1993. Estimating suspended sediment concentrations in surface waters of the Amazon River wetlands from Landsat images. *Remote Sensing of Environment* 43, 281–301.
- Mertes, L., Hickman, M., Waltenberger, B., Bortman, A., Inlander, E., McKenzie, C., Dvorsky, J., 1998. Synoptic views of sediment plumes and coastal geography of the Santa Barbara Channel, California. *Hydrological Processes* 12, 967–979.
- Murray, S., 1972. Observations on wind, tidal and density-driven currents in the vicinity of the Mississippi River delta. In: Swift, D., Duane, D., Pilkey, O. (Eds.), *Shelf Sediment Transport*. Dowden, Hutchinson and Ross, Stroudsburg, PA, pp. 127–142.
- Persson, A., 1998. How do we understand the Coriolis force? *Bulletin of the American Meteorological Society* 79, 1373–1385.
- Persson, A., 2005. The Coriolis effect: four centuries of conflict between common sense and mathematics, part I: a history to 1885. *History of Meteorology* 2, 1–24.
- Phillips, N., 2000. An explication of the Coriolis effect. *Bulletin of the American Meteorological Society* 81 (2), 299–303.
- Preisendorfer, R., 1961. Application of radiative transfer theory to light measurements in the sea. *International Union of Geodesy and Geophysics Monograph* 10, 11–29.
- Press, W., Flannery, B., Teukolsky, S., Vetterling, W., 1990. *Numerical Recipes in C: The Art of Scientific Computing*. Cambridge University Press, Cambridge, 735 pp.
- Rajaratnam, N., 1976. *Turbulent Jets*. Developments in Water Science. Elsevier, Amsterdam, 301 pp.
- Reichardt, H., 1951. Gesetzmässigkeiten der freien turbulenz (Laws of masses of free turbulence). *VDI Forschungsheft* 30, 414.
- Saucier, M. (Ed.), 1998. *Water Resource Development in Louisiana 1998*. U.S. Army Corps of Engineers, New Orleans District, 177 pp.
- Stommel, H., Moore, D., 1989. *An Introduction to the Coriolis Force*. Columbia University Press, New York, 297 pp.
- Stumpf, R., 1987. Remote sensing of suspended sediments in estuaries using atmospheric and compositional corrections to AVHRR data. In: *Proceedings of the 21st International Symposium on Remote Sensing of Environment*. Ann Arbor, Michigan, pp. 205–222.
- Stumpf, R., Pennock, J., 1989. Calibration of a general optical equation for remote sensing of suspended sediments in a moderately turbid estuary. *Journal of Geophysical Research* 94 (C10), 14363–14371.
- Stumpf, R., Pennock, J., 1991. Remote estimation of the diffuse attenuation coefficient in a moderately turbid estuary. *Remote Sensing of Environment* 38, 183–191.
- Syvitski, J., Asprey, K., Clattenburg, D., Hodge, G., 1985. The prodelta environment of a fjord: suspended particle dynamics. *Sedimentology* 32 (1), 83–107.
- Syvitski, J., Skene, K., Nicholson, M., Morehead, M., 1998. *Plume 1.1: Deposition of sediment from a fluvial plume*. *Computers & Geosciences* 24 (2), 159–171.
- Tollmien, W., 1926. Berechnung turbulenter ausbreitungsvorgänge, (Calculation of the turbulent dispersion process). *Zeitschrift fur Angewandte Mathematik und Mechanik* 6, 468–478 (English translation, N.A.C.A. TM 1085, 1945).
- Topliss, B., 1984. Aircraft multispectral remote sensing of suspended sediments in a turbid macrotidal environment. *Mathematical Geology* 16 (7), 719–735.
- Topliss, B., Amos, C., Hill, P., 1990. Algorithms for remote sensing of high-concentration, inorganic suspended s

- ediment. *International Journal of Remote Sensing* 11 (6), 947–966.
- Walker, N., Wiseman Jr., W., Rouse Jr., L., Babin, A., 2005. Effects of river discharge wind stress and slope eddies on circulation of the satellite-observed structure of the Mississippi River plume. *Journal of Coastal Research* 21 (6), 1228–1244.
- Witte, W., Whitlock, C., Ursy, J., Morris, W., Gurganus, E., 1981. Laboratory measurements of physical, chemical and optical characteristics of Lake Chicot sediment waters. NASA Technical Paper 1941.
- Zwillinger, D., 1989. *Handbook of Differential Equations*. Academic Press, Boston, 673 pp.